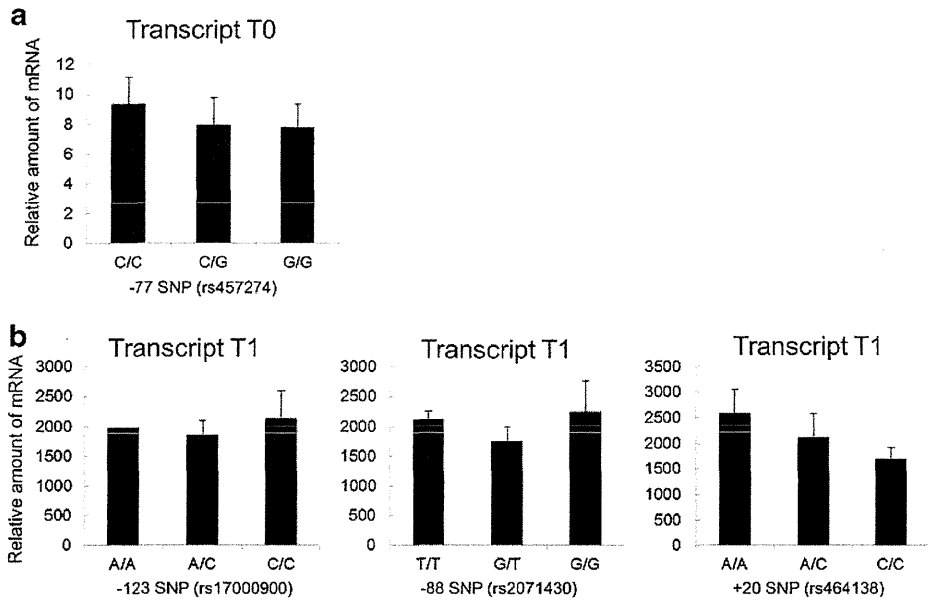

Fig. 5 Differences in the poly(I:C)-induced expression of transcript variants among the genotypes of the promoter and exon 1 SNPs in HBE cells. Expression of **a** T0 and **b** T1 transcripts in the presence of poly(I:C) in HBE cells with each genotype of −77 C/G SNP for the T0 transcript (C/C, n=5; C/G, n=13; G/G, n=11), of −123 C/A SNP (A/A, n=1; A/C, n=12; C/C, n=16), of −88 G/T SNP (T/T, n=2; G/T, n=13; G/G, n=14), and of +20 C/A SNP (A/A, n=3; A/C, n=16; C/C, n=10) for the T1 transcript is shown. The relative amounts of mRNA of each transcript compared with that of the T0 transcript in GG cells without poly(I:C) stimulation are shown as mean±SEM. Possible associations were assessed by a simple regression model (p=0.647 for the number of −77 C alleles, p=0.662 for −123 A alleles, p=0.539 for −88 T alleles, and p=0.331 for +20 A alleles)

T0 transcript. This observation implies that MxA response to viral infection of respiratory cells is mostly controlled by the expression of the T1 transcript.

Remarkably increased levels of the T1 transcript after stimulation with type I IFNs or an IFN-inducing agent, poly(I:C), were consistent with the general consensus that the induction of MxA requires type I or type III IFN signaling (Haller and Kochs 2011). However, levels of the T1 transcript were also elevated in HBE cells by other physiological stimuli. Moderate elevation of levels of the T1 transcript in the presence of IFN-γ and TNF-α may be mediated by the secondary induction of type I or type III IFNs. Although Mahanonda et al. (2012) demonstrated the induction of MxA by α-defensin in primary human gingival epithelial cells, the mechanism by which the T1 transcript was upregulated by α-defensin remains unknown. These observations support the idea that the T1 transcript plays a major role in airway diseases.

We also analyzed the expression of T0 transcript with alternative 5′ untranslated exons. Alternative promoter usage is now recognized as a common mechanism in the transcriptional regulation of mammalian genes (Davuluri et al. 2008). Among IFN-stimulated genes, ADAR1 was shown to have alternative promoters (George and Samuel 1999): one promoter contributes to constitutive expression and the other to inducible expression. To our knowledge, no IFN-stimulated genes other than MxA, whose antiviral function is well known (Sadler and Williams 2008), have been reported to possess two IFN-inducible transcripts with distinct first exons. The molecular mechanism for tissue specificity of these transcripts is unknown; however, of note, the promoter of the T0 transcript contains the putative steroidogenic factor-1 binding site (position −636 to −644) thought to be important to testis- and adrenal gland-specific gene expression (Schimmer and White 2010). A study of the expression profiles of MxA in various organs would be interesting.

Although IFN-mediated upregulation of the T0 transcript was moderate in contrast to that of the T1 transcript, baseline levels of the T0 transcript were not negligible in HBE cells. It is thus conceivable that the T0 transcript plays a minor but independent role in the human airway. Furthermore, considering the difference between the time course of mRNA expression of the T0 and T1 transcripts after poly(I:C) stimulation, it is likely that other factors further modulate their induction levels. Because some reports (Aebi et al. 1989; Goetschy et al. 1989; Prescott et al. 2005) indicate the presence of IFN-independent induction of MxA in contrast to the results of Holzinger et al. (2007), it would be worth investigating whether the T0 transcript can be induced through an IFN-independent signaling system in viral infection.

We observed the regulatory effects of −123, −88, and +20 SNPs on mRNA levels of the T1 transcript in HBE cells

under the unstimulated condition. When we evaluated the overall expression of the MxA transcripts by real-time RT-PCR, it was found to be closely correlated with levels of the T1 transcript, suggesting that individual variation of the total expression of MxA is mainly explained by the T1 transcript. Indeed overall levels of MxA as well as expression of the T1 transcript were strongly associated with these three SNPs at baseline levels. It has been repeatedly reported that the minor A allele of −123 SNP and the minor T allele of −88 SNP, which are in strong LD, were associated with the overall transcriptional activity of the gene (Hijikata et al. 2001; Torisu et al. 2004). Expression of MxA was associated with −88 G/T SNP when PBMC cells were stimulated with IFN-α2 for 12 h (Fernandez-Arcas et al. 2004). In one study (Furuyama et al. 2006), the results of a luciferase reporter assay suggested that −123 SNP contributed to basal expression levels of MxA, whereas −88 SNP contributed to the induction of expression by IFNs. Ching et al. (2010) further showed that the −123A allele had a stronger binding affinity to nuclear proteins from unstimulated cells and that the −88 T allele preferentially bound to the protein after IFN-β stimulation. In our study using HBE cells, −123, −88, and +20 SNPs were all associated with baseline expression of the T1 transcript, and according to a multiple regression analysis, among the three SNPs, +20 C/A SNP was still associated with baseline expression of the T1 transcript. This finding may be attributed to the difference in cell type; however, extensive investigation is required to determine the possible effect of +20 SNP or other unknown functional polymorphisms in strong LD. Recently, Tran Thi Duc et al. (2012) reported that three SNPs (−309 C/G, −101 G/A, and +20 C/A) also contributed to the promoter activity in combination with well-known effects of −123 and −88 SNPs. We could not examine −309 and −101 SNPs in our samples because −309 C/G and −101 G/A SNPs were detected only in the African population and their minor allele frequencies were relatively low (Duc et al. 2012).

Under the poly(I:C)-stimulated condition, the +20 SNP also tended to be associated with expression of the T1 transcript in our study; however, this tendency was not statistically significant. When HBE cells were stimulated with IFN-β for 12 h, the same three SNPs were not associated with the expression level. These findings may conflict with the in vitro effects of these 5′ SNPs on the IFN-inducible promoter activity previously assessed by a luciferase reporter system (Hijikata et al. 2001; Torisu et al. 2004; Tran Thi Duc et al. 2012). In our study, however, the mRNA induced by poly (I:C), the dsRNA analog to mimic viral infection, was directly assessed in primary cultured HBE cells, which implies that individual variance of relevant factors such as toll-like receptor 3 and subsequent IFN signaling pathways might have affected the mRNA levels in the IFN-stimulated condition and have masked the independent effects of these promoter SNPs of the MxA gene.

We previously reported that the promoter −88 SNP was associated with severity of SARS in the Vietnamese population (Hamano et al. 2005), and the promoter −123 SNP was associated with SARS in the Chinese population (Ching et al. 2010). According to Chen and Subbarao (2007), IFN induction is completely suppressed in SARS coronavirus-infected cells. Our ex vivo findings that these regulatory SNPs were mainly involved in baseline expression of the T1 transcript support the results of these disease association studies. However, we could not show significant difference in the regulatory effects between −88 and −123 SNPs, possibly because of strong LD between these two SNPs in the Japanese population (r^2=0.83) compared with moderate LD in the Chinese population (r^2=0.39) (Ching et al. 2010).

In conclusion, we characterized the expression profile of the previously known transcript and the transcript variant of MxA and demonstrated a significant effect of its 5′ SNPs on basal expression of the overall transcripts in HBE cells. Our findings may lead to an improved understanding of the association of MxA SNPs with susceptibility to respiratory viral infections.

Acknowledgments We thank Keiko Wakabayashi for technical assistance in the study. This work was partly supported by a grant from the National Center for Global Health and Medicine.

Conflict of interest All authors have no conflict of interest on this work.

References

Abe H, Hayes CN, Ochi H, Maekawa T, Tsuge M, Miki D, Mitsui F, Hiraga N, Imamura M, Takahashi S, Kubo M, Nakamura Y, Chayama K (2011) IL28 variation affects expression of interferon stimulated genes and peg-interferon and ribavirin therapy. J Hepatol 54:1094–1101

Aebi M, Fah J, Hurt N, Samuel CE, Thomis D, Bazzigher L, Pavlovic J, Haller O, Staeheli P (1989) cDNA structures and regulation of two interferon-induced human Mx proteins. Mol Cell Biol 9:5062–5072

Barrett JC, Fry B, Maller J, Daly MJ (2005) Haploview: analysis and visualization of LD and haplotype maps. Bioinformatics 21:263–265

Chen J, Subbarao K (2007) The immunobiology of SARS. Annu Rev Immunol 25:443–472

Ching JC, Chan KY, Lee EH, Xu MS, Ting CK, So TM, Sham PC, Leung GM, Peiris JS, Khoo US (2010) Significance of the myxovirus resistance A (MxA) gene −123C>a single-nucleotide polymorphism in suppressed interferon beta induction of severe acute respiratory syndrome coronavirus infection. J Infect Dis 201:1899–1908

Davuluri RV, Suzuki Y, Sugano S, Plass C, Huang TH (2008) The functional consequences of alternative promoter use in mammalian genomes. Trends Genet 24:167–177

Duc TT, Farnir F, Michaux C, Desmecht D, Cornet A (2012) Detection of new biallelic polymorphisms in the human MxA gene. Mol Biol Rep 39:8533–8538

Fernandez-Arcas N, Blanco A, Gaitan MJ, Nyqvist M, Alonso A, Reyes-Engel A (2004) Differential transcriptional expresion of

the polymorphic myxovirus resistance protein A in response to interferon-alpha treatment. Pharmacogenetics 14:189–193

Furuyama H, Chiba S, Okabayashi T, Yokota S, Nonaka M, Imai T, Fujii N, Matsumoto H (2006) Single nucleotide polymorphisms and functional analysis of MxA promoter region in multiple sclerosis. J Neurol Sci 249:153–157

George CX, Samuel CE (1999) Human RNA-specific adenosine deaminase ADAR1 transcripts possess alternative exon 1 structures that initiate from different promoters, one constitutively active and the other interferon inducible. Proc Natl Acad Sci U S A 96:4621–4626

Goetschy JF, Zeller H, Content J, Horisberger MA (1989) Regulation of the interferon-inducible IFI-78K gene, the human equivalent of the murine Mx gene, by interferons, double-stranded RNA, certain cytokines, and viruses. J Virol 63:2616–2622

Gray TE, Guzman K, Davis CW, Abdullah LH, Nettesheim P (1996) Mucociliary differentiation of serially passaged normal human tracheobronchial epithelial cells. Am J Respir Cell Mol Biol 14:104–112

Haller O, Kochs G (2011) Human MxA protein: an interferon-induced dynamin-like GTPase with broad antiviral activity. J Interferon Cytokine Res 31:79–87

Hamano E, Hijikata M, Itoyama S, Quy T, Phi NC, Long HT, Ha LD, Ban VV, Matsushita I, Yanai H, Kirikae F, Kirikae T, Kuratsuji T, Sasazuki T, Keicho N (2005) Polymorphisms of interferon-inducible genes OAS-1 and MxA associated with SARS in the Vietnamese population. Biochem Biophys Res Commun 329:1234–1239

Hijikata M, Mishiro S, Miyamoto C, Furuichi Y, Hashimoto M, Ohta Y (2001) Genetic polymorphism of the MxA gene promoter and interferon responsiveness of hepatitis C patients: revisited by analyzing two SNP sites (−123 and −88) in vivo and in vitro. Intervirology 44:379–382

Hijikata M, Ohta Y, Mishiro S (2000) Identification of a single nucleotide polymorphism in the MxA gene promoter (G/T at nt −88) correlated with the response of hepatitis C patients to interferon. Intervirology 43:124–127

Holzinger D, Jorns C, Stertz S, Boisson-Dupuis S, Thimme R, Weidmann M, Casanova JL, Haller O, Kochs G (2007) Induction of MxA gene expression by influenza A virus requires type I or type III interferon signaling. J Virol 81:7776–7785

Horisberger MA, McMaster GK, Zeller H, Wathelet MG, Dellis J, Content J (1990) Cloning and sequence analyses of cDNAs for interferon- and virus-induced human Mx proteins reveal that they contain putative guanine nucleotide-binding sites: functional study of the corresponding gene promoter. J Virol 64:1171–1181

Kong XF, Zhang XX, Gong QM, Gao J, Zhang SY, Wang L, Xu J, Han Y, Jin GD, Jiang JH, Zhang DH, Lu ZM (2007) MxA induction may predict sustained virologic responses of chronic hepatitis B patients with IFN-alpha treatment. J Interferon Cytokine Res 27:809–818

Leong DT, Gupta A, Bai HF, Wan G, Yoong LF, Too HP, Chew FT, Hutmacher DW (2007) Absolute quantification of gene expression in biomaterials research using real-time PCR. Biomaterials 28:203–210

Mahanonda R, Sa-Ard-Iam N, Rerkyen P, Thitithanyanont A, Subbalekha K, Pichyangkul S (2012) MxA expression induced by alpha-defensin in healthy human periodontal tissue. Eur J Immunol 42:946–956

McGilvray I, Feld JJ, Chen L, Pattullo V, Guindi M, Fischer S, Borozan I, Xie G, Selzner N, Heathcote EJ, Siminovitch K (2012) Hepatic cell-type specific gene expression better predicts HCV treatment outcome than IL28B genotype. Gastroenterology 142:1122–1131

Peng XM, Lei RX, Gu L, Ma HH, Xie QF, Gao ZL (2007) Influences of MxA gene−88 G/T and IFN-gamma +874 A/T on the natural history of hepatitis B virus infection in an endemic area. Int J Immunogenet 34:341–346

Prescott J, Ye C, Sen G, Hjelle B (2005) Induction of innate immune response genes by Sin Nombre hantavirus does not require viral replication. J Virol 79:15007–15015

Randall RE, Goodbourn S (2008) Interferons and viruses: an interplay between induction, signalling, antiviral responses and virus countermeasures. J Gen Virol 89:1–47

Ronni T, Matikainen S, Lehtonen A, Palvimo J, Dellis J, Van Eylen F, Goetschy JF, Horisberger M, Content J, Julkunen I (1998) The proximal interferon-stimulated response elements are essential for interferon responsiveness: a promoter analysis of the antiviral MxA gene. J Interferon Cytokine Res 18:773–781

Sadler AJ, Williams BR (2008) Interferon-inducible antiviral effectors. Nat Rev Immunol 8:559–568

Schimmer BP, White PC (2010) Minireview: steroidogenic factor 1: its roles in differentiation, development, and disease. Mol Endocrinol 24:1322–1337

Torisu H, Kusuhara K, Kira R, Bassuny WM, Sakai Y, Sanefuji M, Takemoto M, Hara T (2004) Functional MxA promoter polymorphism associated with subacute sclerosing panencephalitis. Neurology 62:457–460

Tran Thi Duc T, Desmecht D, Cornet A (2012) Functional characterization of new allelic polymorphisms identified in the promoter region of the human MxA gene. Int J Immunogenet. doi:10.1111/j.1744-313X.2012.01153.x

ORIGINAL ARTICLE

Epigenetic Regulation of Adipogenesis by PHF2 Histone Demethylase

Yosuke Okuno,[1] Fumiaki Ohtake,[1] Katsuhide Igarashi,[2] Jun Kanno,[2] Takahiro Matsumoto,[1] Ichiro Takada,[1] Shigeaki Kato,[3] and Yuuki Imai[1]

PHF2 is a JmjC family histone demethylase that removes the methyl group from H3K9me2 and works as a coactivator for several metabolism-related transcription factors. In this study, we examined the in vivo role of PHF2 in mice. We generated *Phf2* floxed mice, systemic *Phf2* null mice by crossing *Phf2* floxed mice with *CMV-Cre* transgenic mice, and tamoxifen-inducible *Phf2* knockout mice by crossing *Phf2* floxed mice with *Cre-ERT2* transgenic mice. Systemic *Phf2* null mice had partial neonatal death and growth retardation and exhibited less adipose tissue and reduced adipocyte numbers compared with control littermates. Tamoxifen-induced conditional knockout of PHF2 resulted in impaired adipogenesis in stromal vascular cells from the adipose tissue of tamoxifen-inducible *Phf2* knockout mice as well as of *Phf2* knocked-down 3T3-L1 cells. PHF2 interacts with CEBPA and demethylates H3K9me2 in the promoters of CEBPA-regulated adipogenic genes. These findings suggest that PHF2 histone demethylase potentiates adipogenesis through interaction with CEBPA in vivo. Taken together, PHF2 may be a novel therapeutic target in the treatment of obesity and the metabolic syndrome.

The architecture of eukaryotic chromatin is dynamically modulated by posttranslational modifications of the histones, including acetylation, phosphorylation, ubiquitination, and methylation (1). Methylation states of histones are crucial for chromatin reorganization and regulation of gene transcription. For example, lysine (K) methylation at H3K9, H3K27, and H4K20 is associated with regions of transcriptionally silenced chromatin, whereas methylation at H3K4, H3K36, and H3K79 is associated with transcriptionally active regions. Such modifications are controlled by a balance between enzymes that catalyze the addition and removal of methyl groups. LSD1 and the Jumonji C (JmjC) domain–containing proteins have been shown to possess such histone demethylase activities (2–4).

Plant homeodomain finger 2 (PHF2) is a newly characterized JmjC domain–containing protein identified as an interactant of nuclear receptors. PHF2 forms a complex with the AT-rich interactive domain 5B (ARID5B) and works as a coactivator for farnesoid X receptor (FXR) or hepatocyte nuclear factor 4 α (HNF4A). It is enzymatically inactive by itself but becomes an active H3K9me2 demethylase through protein kinase A (PKA)-mediated phosphorylation (5).

Although an increasing number of histone demethylases have been identified and their molecular functions progressively unraveled, the physiological functions of these demethylases remain largely unknown. Recently, LSD1 was reported to be required for embryogenesis (6), whereas JHDM2A is required for spermatogenesis (7) and obesity resistance (8) in vivo. In zebra fish, PHF8 and KDM7, which belong to the same subfamily of JmjC domain proteins as PHF2, regulate brain development (9,10). It has been suggested that PHF2 plays a role in induction of gluconeogenic genes by PKA signaling in hepatocytes (5) or rRNA expression in nucleoli (11) in vitro. However, in vivo analyses are required to explore the physiological role of PHF2. In this study, we generated PHF2 knockout mice and found that PHF2 plays a role in both neonatal growth and adipogenesis. These results imply that PHF2 demethylase function would be a novel translational target for human metabolic diseases.

RESEARCH DESIGN AND METHODS

Generation of *Phf2* floxed mice by gene targeting. A bacterial artificial chromosome (BAC) DNA containing mouse *Phf2* (BAC clone RP23-114C14) was obtained from the BAC-PAC Resources Center. *LoxP* was inserted between exons 6 and 7 of *Phf2* using the *Escherichia coli*-based BAC modification system (12). Modification cassettes were generated by PCR amplification of the PL452 vector with the following primers:5′-TATATAAGGAGCACTTGGGACCAGT GACATACATGTGTCTAATGTCCTGAGAATTCATTCCGATCATATTCAATAACCC-3′ and 5′-ACTCTGGACACTAGGTGACCCAGTGGCCTCTCCTAATAGTTAATGA GCTCGAACTAGTGGATCCCCTCGA-3′. *LoxP*-inserted fragments of mouse *Phf2* were subcloned into the pBSIIKS+ vector using the *E. coli*-based BAC recombination system. Modification cassettes and retrieval cassettes were generated by PCR amplification of the pBSIIKS+ vector with primers corresponding to each promoter. *LacZ-PGK-Neo* was digested from the pNTR-lacZ-PGK-neo-lox vector and inserted into the pMC1DTpA vector that contained *DT-A*. Oligonucleotides of *loxP* and *frt* were inserted into this vector (cassette vector). *LoxP*-inserted fragments of mouse *Phf2* were inserted into the cassette vector to form the final *Phf2* knockout construct. The *Phf2* knockout construct was linearized by SacII and was introduced into M1 mouse embryonic cells (RIKEN) by electroporation and screened by genomic Southern blotting. Chimeric mice were generated by aggregation of embryonic stem cells with eight cell embryos of BDF1 mice. $Phf2^{Z/+}$ mice were generated by crossing $Phf2^{Nf/+}$ mice with *CMV-Cre* mice (13). $Phf2^{fl/+}$ mice were generated by crossing $Phf2^{Nf/+}$ mice with Flpe deleter strain ACTB-Flpe mice (Jackson Laboratory). Mice with $Phf2^{Nf/+}$, $Phf2^{Z/+}$, and $Phf2^{fl/+}$ were maintained by backcrossing to C57BL/6J mice under a specific pathogen-free environment. All animals were maintained according to the protocol approved by the Animal Care and Use Committee of The University of Tokyo.

Generation of *Phf2* conditional knockout mice and genotyping. *Cre-ERT2* transgenic mice were provided by Dr. Daniel Metzger (14). *Cre-ERT2* transgenic mice were crossed with $Phf2^{fl/+}$ mice to generate $Phf2^{fl/fl}$;*Cre-ERT2* mice. Genotyping was performed by PCR using corresponding primers. Sequences of primers were as follows: P1, 5′-CACCCTCTGTGTCCTCCTGT-3′; P2, 5′-CAGTTCTCTTAGCTCCCCCTTT-3′; P3, 5′-GACAGGAAGCCAAGGAGATG-3′; P4, 5′-GACAGCCTGGTCAGGTGAAT-3′; and P5, 5′-TGTAATACACCTGGGGCTCA-3′. *Cre-ERT2* transgenic mice were identified by amplification of the *Cre* allele using primers 5′-TTACGGCGCTAAGGATGACT-3′ and 5′-TTGCCCCTGTTTCACTATCC-3′.

From the [1]Laboratory of Epigenetic Skeletal Diseases, Institute of Molecular and Cellular Biosciences, The University of Tokyo, Tokyo, Japan; the [2]Division of Cellular and Molecular Toxicology, National Institute of Health Sciences, Tokyo, Japan; and the [3]Soma Central Hospital, Soma, Japan.
Corresponding author: Yuuki Imai, yimai@iam.u-tokyo.ac.jp.
Received 15 May 2012 and accepted 5 November 2012.
DOI: 10.2337/db12-0628
This article contains Supplementary Data online at http://diabetes.diabetesjournals.org/lookup/suppl/doi:10.2337/db12-0628/-/DC1.

Adipose tissue collection. Mice were killed by cervical dislocation. Epididymal, gonadal, lumbar subcutaneous, and mesenteric white adipose tissues (WATs) were carefully separated from testis, uterus, skin, and intestines, respectively. Wet weights of these WATs were measured.

Glucose and insulin tolerance tests. Food was removed 2 h before glucose (2 g/kg) or insulin (1 units/kg) was administered by intraperitoneal injection. Blood samples were collected from the tail vein at various times after the glucose load, as indicated. Plasma glucose was immediately determined on an Accu-Chek Aviva (Roche).

Cell culture. 3T3-L1 mouse fibroblasts were maintained and differentiated into adipocytes as previously described (15). Mouse primary embryonic fibroblasts were isolated on embryonic day 13.5 and cultured in Dulbecco's modified Eagle's medium with 10% FBS.

Plasmids. FLAG-tagged, full-length cDNAs of human CEBPA or PPARG were inserted into pcDNA3 vectors (Invitrogen).

Western blot. Protein levels were determined by blotting with anti-FLAG antibody (Sigma-Aldrich), anti-CEBPA antibody (Santa Cruz Biotechnology), and anti-PHF2 antibody (5). ECL Plus (Amersham) was used for detection of the immunoreactive bands.

mRNA analysis. Total RNA was isolated with TRIzol reagent (Invitrogen) according to the manufacturer's protocol. First-strand cDNA was synthesized from total RNA using PrimeScript RT Master Mix (Takara) and subjected to real-time PCR using KAPA SYBR Fast qPCR Kits (Kapa Biosystems) with Thermal Cycler Dice (Takara) according to the manufacturers' instructions. The following primers were used: mouse *Phf2*, 5′-TACTGCCTGATCTGTGTGAAGGA-3′ and 5′-CTGGCCGGATGAGATAGAAGA-3′; mouse *Pparg*, 5′-TTAACTGCCGGATCCACAAAA-3′ and 5′-TGAGACATCCCCACAGCAAG-3′; mouse *Cebpa*, 5′-TGCCAAACTGAGACTCTTCACTAAC-3′ and 5′-CCCAAACATCCCTAAACCAAAA-3′; mouse *Adipoq*, 5′-CAAGGCCGTTCTCTTCACCTAC-3′ and 5′-TCCCCATCCCCATACACCT-3′; mouse *Fabp4*, 5′-CAGCGTAAATGGGGATTTGG-3′ and 5′-GCTCTTCACCTTCCTGTCGTCT-3′; mouse *Plin2*, 5′-GAGCTGGAGATGGAAGCAAAA-3′ and 5′-GTGATAAGCCCGAGAGCAGAG-3′; mouse *Cd36*, 5′-AAGAACAGCAGCAAAATCAAGG-3′ and 5′-AGACAGTGAAGGCTCAAAGATGG-3′; mouse *Lpl*, 5′-TGGGACTGAGGATGGCAAG-3′ and 5′-GGCAGGGTGAAGGGAATGT-3′; and mouse *Arbp*, 5′-GCTCCAAGCAGATGCAGCA-3′ and 5′-CCGGATGTGAGGCAGCAG-3′.

Retroviral infection. Platinum-E cells were transfected with either pSuper-retro-puro-shLacZ or pSuper-retro-puro-shPHF2 (5′-GCCTGACTCAGTTTCCCAACT-3′) using Lipofectamine (Invitrogen). Forty-eight hours after transfection, the medium containing retroviruses was harvested, filtered, and transferred to 3T3-L1 cells. Infected cells were selected with 1 μg/mL puromycin.

Chromatin immunoprecipitation assays. Chromatin immunoprecipitation (ChIP) assays were carried out essentially as previously described (16). For immunoprecipitation, antibody against CEBPA (sc-61; Santa Cruz Biotechnology) or PHF2 (5) was used. The precipitated DNA fragments were amplified by real-time PCR. The following primers were used: mouse *Cebpa*-CEBPRE, 5′-TTGCGCCACGATCTCTCTC-3′ and 5′-CTTAGAGCCCGCCTTCTCCT-3′; mouse *Pparg*-CEBPRE, 5′-CCACTGGTGTGTATTTTACTGCAA-3′ and 5′-GTTCTGTGAGGGGCGTGAA-3′; mouse *Fabp4*-CEBPRE, 5′-CATTGCCAGGGAGAACCAA-3′ and 5′-CCATGTGACTGTAGGAGTGACCAA-3′; and mouse negative control region, 5′-CAGACATGTCAAATCAAGAAGACAG-3′ and 5′-ACTTTGGAGGAAGAGGCAGAAA-3′.

Microarray analysis. These procedures were conducted according to the Percellome method (17). Briefly, mRNA expression values were normalized to the cell numbers in each sample by adding external spike mRNAs to them in proportion to the genomic DNA concentration and using the spike RNA quantity data as a dose-response standard curve for each sample. Total RNAs were purified from epididymal adipose tissue using an RNeasy Mini kit (Qiagen). First-strand cDNAs were synthesized using SuperScript II reverse transcriptase (Invitrogen). After second-strand synthesis, the double-stranded cDNAs were purified using a GeneChip (Affymetrix) Sample Cleanup Module and labeled by in vitro transcription using a BioArray HighYield RNA Transcript Labeling Kit (Enzo Life Sciences). The labeled cRNA was then purified using a GeneChip Sample Cleanup Module. Purified cRNA were hybridized with GeneChip Mouse Genome 430 2.0 Array. Washing and staining were performed in a GeneChip Fluidics Station using the appropriate antibody amplification, washing, and staining protocols. The phycoerythrin-stained arrays were scanned as digital image files, which were analyzed with GeneChip Operating Software. The expression data were converted to copy numbers of mRNA per cell by the Percellome method and analyzed using Percellome software.

Morphometric analysis. Paraffin sections of epididymal WAT were processed for hematoxylin-eosin staining and observed by light microscopy. Adipocyte areas were measured using OsteoMeasure.

Evaluation of adipocyte number. The number of adipocytes in epididymal WAT was estimated as previously described (18). Briefly, adipose tissue was minced and fixed at 37°C for 96 h in 1.88% osmium tetroxide. After washing twice with PBS, it was replaced with 8 mol/L urea at room temperature for 48 h. Urea-free particles were washed through a 180-μm net (Millipore), trapped on a 10-μm net (Millipore), and suspended using 0.01% Triton X-100 in PBS. Particles were counted with a counting chamber.

Oil red O staining. Cells were stained with oil red O, and the quantification was performed as previously described (19). Briefly, cells were fixed with 10% formalin and stained in a working solution of oil red O. Isopropyl alcohol was added to the stained culture dishes, and the extracted dye was monitored spectrophotometrically at 510 nm.

Statistical analysis. Data were analyzed by two-tailed Student *t* test, Pearson χ^2 test, log-rank test, or two-way repeated-measures ANOVA. For all graphs, data are presented as mean ± SEM. Statistical significance was accepted at $P < 0.05$.

RESULTS

Generation of *Phf2* floxed mice. Figure 1*A* shows the strategy to generate the mutant *Phf2* mutant allele. Successful insertion of *LacZ-PGK-Neo*^{R} cassettes and *loxP* at sites flanking exon 6 of the *Phf2* allele was confirmed by Southern blotting (Fig. 1*B*). Cre-mediated recombination excised exon 6 and *PGK-Neo*^{R} from the mutant allele, resulting in the *LacZ* allele. P1, P2, and P3 primers were used to differentiate the wild-type and *LacZ* alleles (Fig. 1*C*). Flpe-mediated recombination excised *LacZ* and *PGK-Neo*^{R} from the mutant allele, resulting in a floxed allele. P4 and P5 primers were used to differentiate the wild-type and floxed alleles (Fig. 1*D*). Cre-mediated recombination excised exon 6 from the floxed allele, resulting in a null allele. Exon 6 corresponds to part of the JmjC domain of *Phf2*, and its deletion is expected to result in an alteration of the reading frame of the *Phf2* transcript. As expected, the PHF2 protein was not detected in mouse embryonic fibroblasts of *Phf2*$^{Z/Z}$ (Fig. 1*E*).

***Phf2*$^{Z/Z}$ mice were characterized by partial neonatal death and postnatal growth retardation.** *Phf2*$^{Z/Z}$ mice were born according to expected Mendelian ratios (Fig. 2*A*). However, <30% of *Phf2*$^{Z/Z}$ pups were alive when they reached 2 weeks of age (Fig. 2*B*). In fact, daily observation revealed that ~70% of *Phf2*$^{Z/Z}$ mice died within 3 days of birth ($P = 3.0 \times 10^{-5}$ compared with wild type) (Fig. 2*C*). However, after 3 days of age, the remaining pups retained viability and lived for no less than 6 months (data not shown). *Phf2*$^{Z/Z}$ mice had progressively reduced growth compared with littermate controls until 10 days after birth, although there was little difference in body weight among newborn mice of different genotypes (Fig. 2*D*). Two weeks after birth, *Phf2*$^{Z/Z}$ mice grew in a manner similar to wild-type or heterozygous littermates, but with significant differences in body weight (Fig. 2*E*). The extent of these weight reductions was not significantly different between males and females (two-way repeated-measures ANOVA). These data suggest that PHF2 is dispensable for the survival of embryos but is necessary for survival and growth in the neonatal period.

Reduced adipose tissue in *Phf2*$^{Z/Z}$. Next, we surveyed the weight and appearance of each tissue present in male *Phf2*$^{Z/Z}$ mice at 5 weeks of age. As mentioned previously, *Phf2*$^{Z/Z}$ mice had decreased body weights at that time (Fig. 3*A*). *Phf2*$^{Z/Z}$ mice exhibited significantly shortened body lengths (Fig. 3*A*). Various tissues of *Phf2*$^{Z/Z}$, including brown adipose tissue (BAT), appeared normal and weighed the same as in control littermates. However, WAT and brain showed a different trend. The brain weights were significantly increased compared with wild-type littermates, the potential significance of which will be discussed later (Fig. 3*A*). The weight of epididymal WAT was only 50% of that found in control littermates, even when normalized by body weight. Weight reduction was also

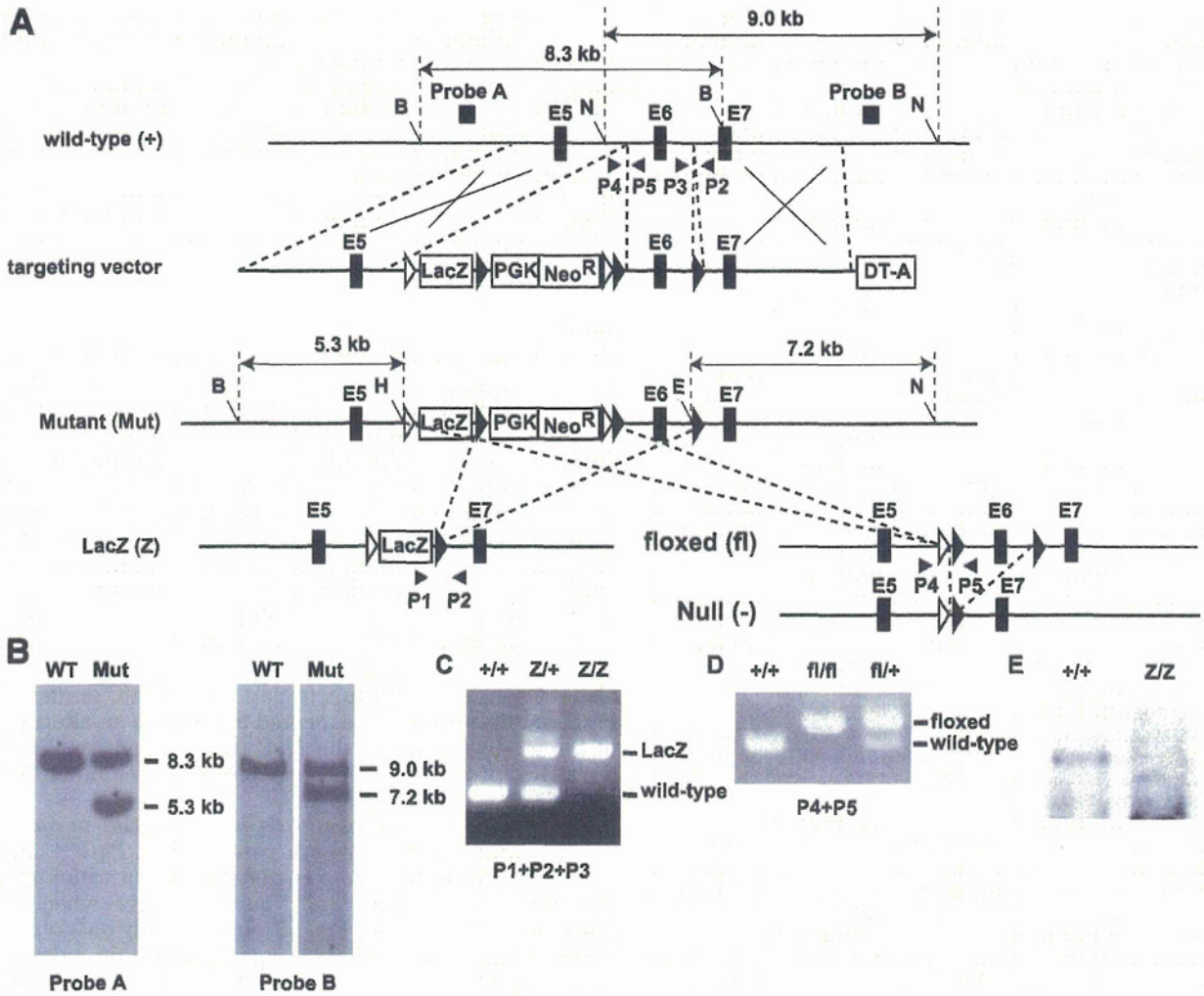

FIG. 1. Strategic scheme for targeted disruption of mouse *Phf2*. *A*: Targeting strategy with positive/negative selection. Strategy of genomic Southern blotting in the screening for homologous recombinant embryonic stem cell clones is also included. E5, E6, and E7 represent exon 5, exon 6, and exon 7 of *Phf2*, respectively. B, H, E, and N represent BglII, HindIII, EcoRI, and NsiI cut sites, respectively. P1, P2, P3, P4, and P5 represent locations of primers used in *C* and *D*. ▷, the *LoxP* sites; ▶, *Frt* sites. *B*: Southern blotting analysis of targeted embryonic stem cell clones. Restriction enzymes used for screening recombination events with probe A were BglII and HindIII. An 8.3-kb fragment in WT and a 5.3-kb fragment after homologous recombination were expected with probe A. Restriction enzymes used for screening recombination events with probe B were EcoRI and NsiI. A 9.0-kb fragment in WT and a 7.2-kb fragment after homologous recombination were expected with probe B. *C*: To detect the presence of the *LacZ* allele (Z) and the WT allele (+),primers P1, P2, and P3 were used. The PCR bands of the WT allele (242 bp) and the *LacZ* allele (495 bp) are indicated. *D*: To detect the presence of the floxed allele (*fl*) and the WT allele (+),primers P4 and P5 were used. The PCR bands of the WT allele (162 bp) and the floxed allele (245 bp) are indicated. *E*: Western blot analysis of PHF2 protein expression in $Phf2^{Z/Z}$ mice. Extracts of mouse embryonic fibroblasts from WT or $Phf2^{Z/Z}$ were immunoprecipitated and detected with anti-PHF2 antibody. WT, wild type.

observed in subcutaneous WAT to an extent similar to that in epididymal WAT (P = 0.06) but to a lesser extent in mesenteric WAT (Fig. 3*B*). Additionally, female $Phf2^{Z/Z}$ mice exhibited a similar reduced weight of gonadal WAT as observed in male mice (Fig. 3*C*). However, these weight reductions in adipose tissues seemed to be limited to a young age because there was no significant difference of WAT weights between $Phf2^{Z/Z}$ and wild-type littermates when the mice reached 8 weeks of age (Supplementary Fig. 1). To elucidate whether the decreased weight of WAT was caused by a reduction of lipid droplets per cell or adipocyte number, we measured adipocyte size and number in epididymal WAT of $Phf2^{Z/Z}$ and wild-type littermates. Evaluation of the mean adipocyte area in the section of WAT revealed that $Phf2^{Z/Z}$ mice have smaller adipocytes than do control littermates (Fig. 3*D*). Furthermore, counting the number of adipocytes in WAT revealed that $Phf2^{Z/Z}$ mice have fewer adipocytes in adipose tissue (Fig. 3*E*). These data suggest that the decreased weight of WAT in $Phf2^{Z/Z}$ mice was caused by a reduction in both the size and the number of adipocytes. Because impaired adipogenesis often results in decreased size (20) and a decreased number of adipocytes, we used microarray analysis to compare the gene expression profiles in WAT between $Phf2^{Z/Z}$ mice and control littermates. As a result, the expression of various genes associated with adipogenesis, such as *Pparg*, *Cebpa*, *Fabp4*, *Adipoq*, *LPL*, *Plin2*, and *Cd36*, tended to be decreased in $Phf2^{Z/Z}$ mice (Supplementary Fig. 2). The expression levels of more than half of these genes were significantly reduced when confirmed by real-time quantitative PCR (qPCR) (Fig. 3*F*). These data suggest that decreased WAT weight in $Phf2^{Z/Z}$ mice resulted, at least in part, from impaired adipogenesis in these mice. Finally, we measured insulin sensitivity in

A At Birth

+/+	Z/+	Z/Z	Total
9	14	11	34
26%	41%	32%	100%

B At 2 weeks

+/+	Z/+	Z/Z	Total
52	91	17**	160
33%	57%	11%	100%

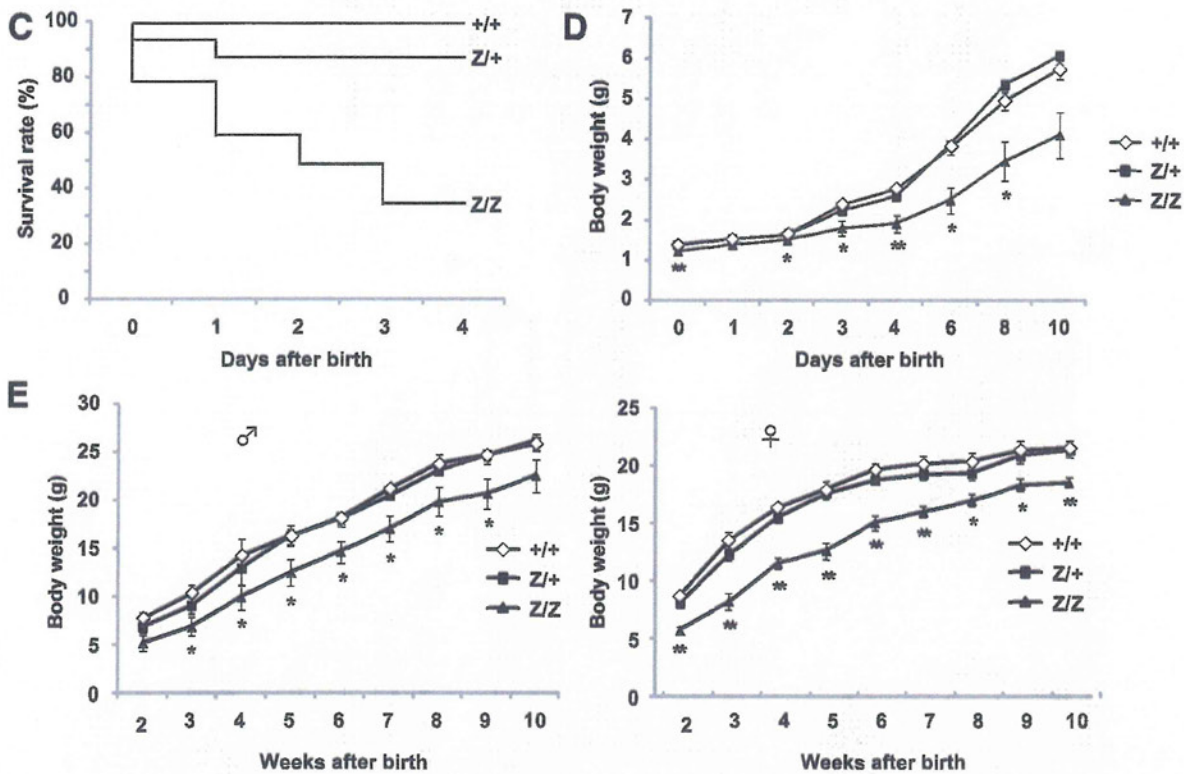

FIG. 2. Physiological features of systemic *Phf2* knockout mice. *A*: Genotypes of progeny of crosses between $Phf2^{Z/+}$ at birth. *B*: Genotypes of progeny of crosses between $Phf2^{Z/+}$ at 2 weeks of age. *C*: Survival rate of progeny of crosses between $Phf2^{Z/+}$. *D*: Growth curves of wild-type, heterozygous, and homozygous *Phf2* knockout mice until 10 days after birth. *E*: Growth curves of male mice and female mice of indicated genotypes between 2 and 10 weeks of age. ◇, wild-type mice (+/+); ■, heterozygous *Phf2* knockout mice (*Z*/+); ▲, homozygous *Phf2* knockout mice (*Z*/*Z*). *$P < 0.05$; **$P < 0.01$ compared with wild type.

$Phf2^{Z/Z}$ mice because adipose tissue is well known to be involved in glucose metabolism. There was no significant change in the glucose or insulin tolerance tests (Supplementary Fig. 3), suggesting that reduced WAT weight did not affect insulin sensitivity in mice at 5 weeks of age.

PHF2 is necessary for normal adipogenesis. To elucidate the role of PHF2 in adipogenesis, we generated $Phf2^{fl/fl}$;*Cre-ERT2* mice by crossing *Phf2* floxed mice with *Cre-ERT2* mice. Stromal vascular cells (SVCs) were then obtained from $Phf2^{fl/fl}$;*Cre-ERT2* mice or control *Cre-ERT2* mice and treated with 4-hydroxytamoxifen (4-OHT) to induce Cre-mediated excision of *Phf2*. As expected, treatment with 4-OHT efficiently reduced mRNA expression of *Phf2* in $Phf2^{fl/fl}$;*Cre-ERT2* but not in control *Cre-ERT2* mice (Fig. 4*C*). When SVCs were treated with a differentiation cocktail to induce their differentiation into adipocytes, differentiation was impaired in 4-OHT-treated SVCs from $Phf2^{fl/fl}$;*Cre-ERT2* mice as shown by oil red O staining (Fig. 4*A* and *B*). This was also confirmed by decreased expression of adipogenic marker genes in 4-OHT–treated SVCs from $Phf2^{fl/fl}$;*Cre-ERT2* mice (Fig. 4*C*). Next, we generated 3T3-L1 cell lines in which PHF2 was stably knocked down by retrovirus carrying *Phf2*-targeted short hairpin RNA. Infection of retrovirus carrying *shPhf2* successfully decreased the expression of *Phf2* (Fig. 4*F*). In accordance with the results from SVCs, short hairpin RNA-mediated knockdown of *Phf2* resulted in impaired adipogenesis in the 3T3-L1 cell line as assessed by oil red O staining (Fig. 4*D* and *E*) and expression of adipogenic marker genes (Fig. 4*F*).

PHF2 is recruited with CEBPA to the promoter regions of adipogenic genes. The results indicated that PHF2 promoted adipogenesis. Moreover, we show that PHF2 works as a coactivator for several transcription factors through H3K9me2 demethylation (5). Therefore, we hypothesized that PHF2 coactivates transcription factors that promote adipogenesis. Among such transcription factors, PPARG and CEBPA are the master regulators for adipogenesis (21). First, we assessed whether PHF2 could physically interact with PPARG or CEBPA. When transfected into HEK293 cells, FLAG-CEBPA (but not FLAG-PPARG) was coimmunoprecipitated with endogenous PHF2 (Fig. 5*A*). Conversely, FLAG-PHF2 was coimmunoprecipitated with endogenous CEBPA in 3T3-L1 adipocytes (Fig. 5*B*). In accordance with these results, ChIP analysis revealed that PHF2 was recruited to known CEBPRE (CEBP responsive elements) in the promoter regions of *Cebpa*, *Pparg*, and *Fabp4* in differentiated

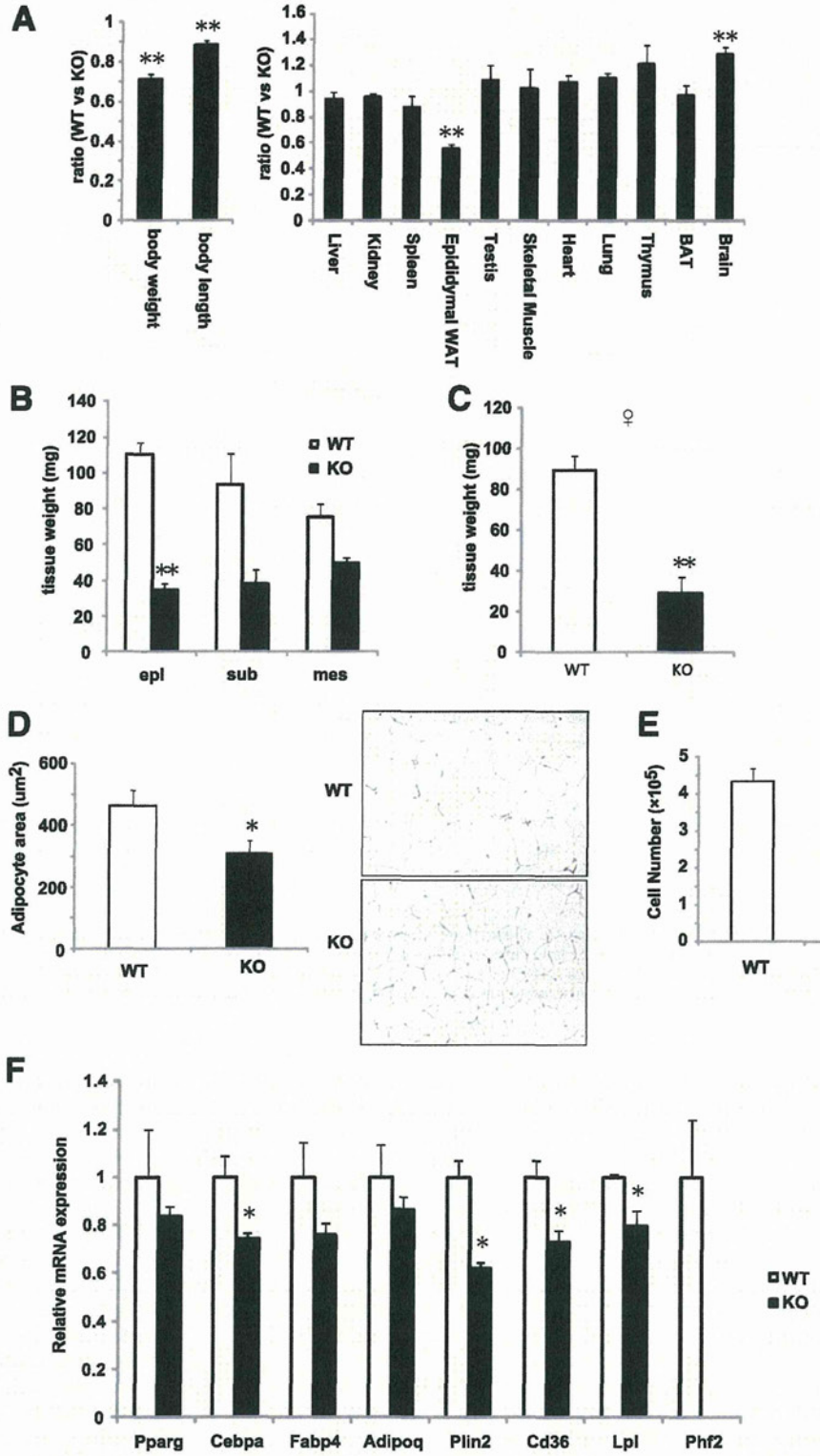

FIG. 3. Assessment of adipose tissue of systemic *Phf2* knockout mice. *A*: Ratio of body weight and nasoanal length or normalized tissue weight of male $Phf2^{Z/Z}$ to WT littermates at 5 weeks of age. Tissue weights were normalized to body weights (n = 6). *B*: Weights of epididymal WAT, subcutaneous WAT, and mesenteric WAT of male $Phf2^{Z/Z}$ KO mice and WT littermates at 5 weeks of age (n = 3). *C*: Weights of gonadal WAT of female $Phf2^{Z/Z}$ KO mice and WT littermates at 5 weeks of age (n = 4). *D*: Mean adipocyte areas of epididymal WAT from $Phf2^{Z/Z}$ KO mice and WT littermates (n = 5). High-magnification micrographs of WAT are shown. *E*: Adipocyte number in epididymal fat pads of $Phf2^{Z/Z}$ KO mice and WT littermates (n = 7). *F*: Real-time qPCR analysis of adipocyte marker genes and *Phf2* of $Phf2^{Z/Z}$ KO mice and WT littermates (n = 3). *$P < 0.05$; **$P < 0.01$ compared with WT. KO, knockout; WT, wild type. (A high-quality color representation of this figure is available in the online issue.)

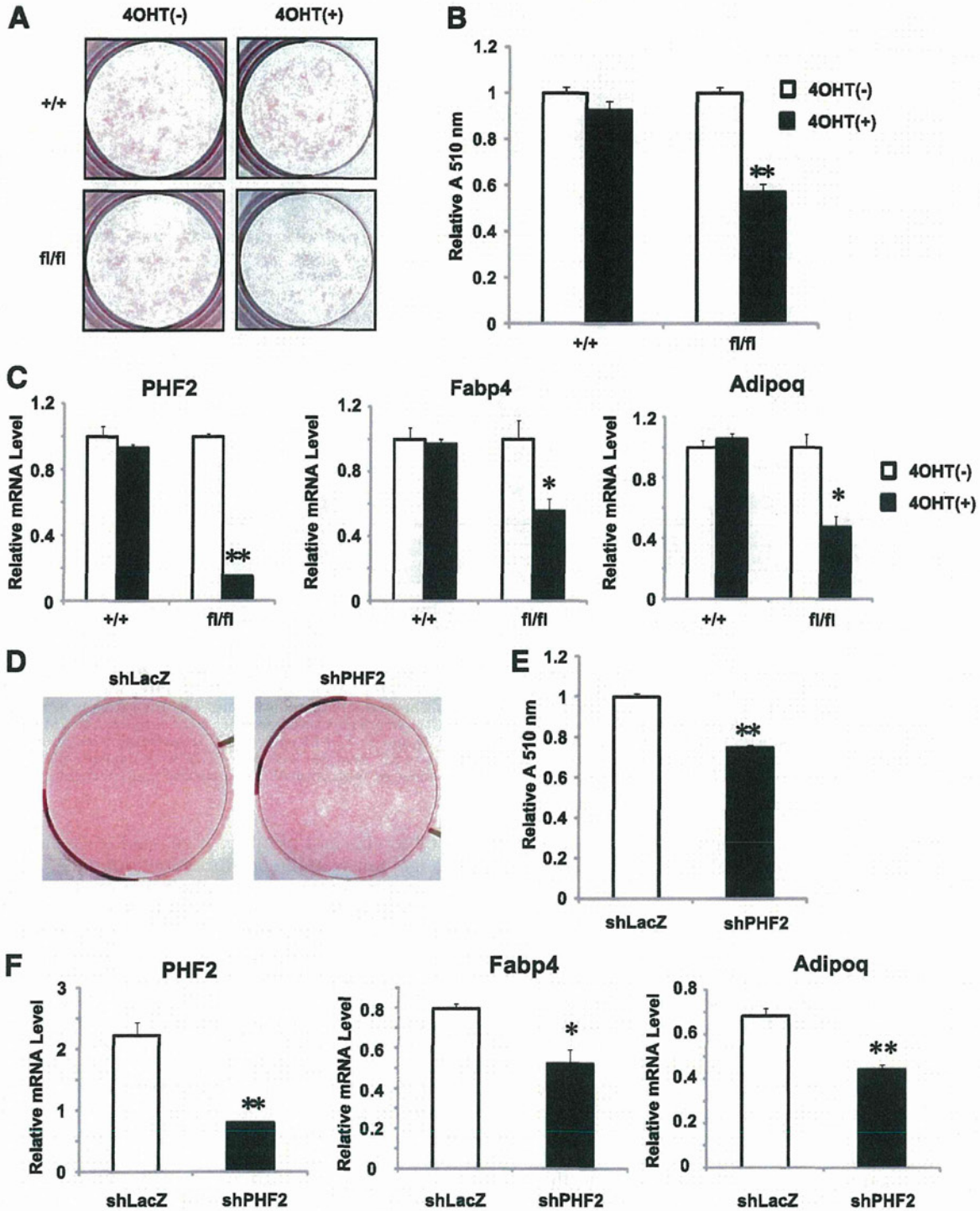

FIG. 4. Effects of PHF2 knock down on adipogenesis. *A–C*: SVCs from *Cre-ERT2; Phf2*$^{fl/fl}$ (*fl/fl*) or *Cre-ERT2* (+/+) were treated with or without 4-OHT and differentiated into adipocytes by treatment with insulin, dexamethasone, and isobutylmethylxanthine. Image (*A*) and quantification (*B*) of oil red O staining and the results of real-time qPCR analysis of adipocyte marker genes (*C*) are shown (n = 3). *D–F*: 3T3-L1 cells infected with retroviruses containing either pSuper-retro-shLacZ or pSuper-retro-shPHF2 were differentiated into adipocytes. Image (*D*) and quantification (*E*) of oil red O staining and the results of real-time qPCR analysis of adipocyte marker genes (*F*) are shown (n = 3). *P < 0.05; **P < 0.01 compared with control.

3T3-L1 adipocytes (Fig. 5*C*). These results indicate that PHF2 might work as a coactivator for CEBPA. PHF2 seemed to be necessary for recruitment of CEBPA to chromatin because the recruitment of CEBPA to CEBPRE was impaired in 3T3-L1 in which *Phf2* had been knocked down (Fig. 5*D*). Moreover, modification of H3K9me2 in these CEBPRE was significantly increased in *Phf2* knocked-down 3T3-L1 adipocytes (Fig. 5*E*). These data indicate that PHF2 can play

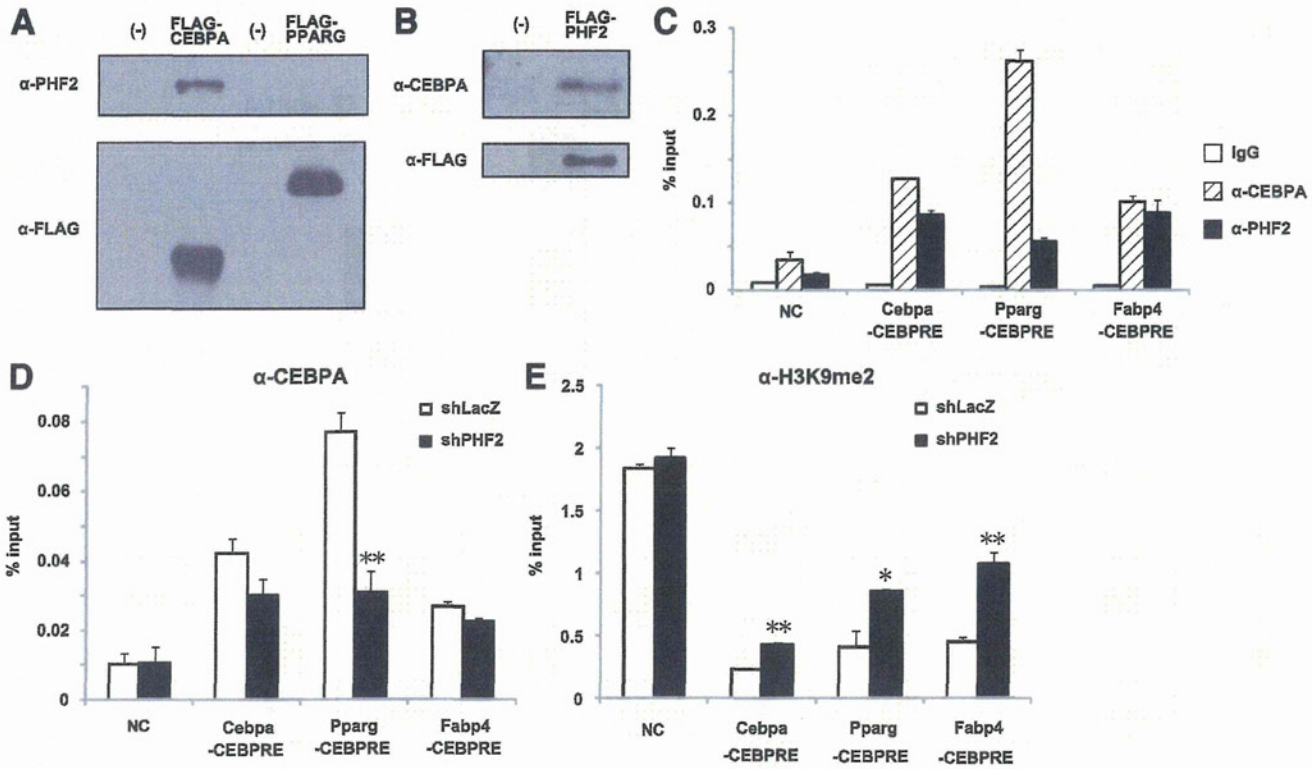

FIG. 5. Association of PHF2 with CEBPA. *A*: FLAG-CEBPA or FLAG-PPARG was transfected into HEK293T cells. Cells were harvested and immunoprecipitated with anti-FLAG antibody and detected with anti-PHF2 antibody or anti-FLAG antibody. *B*: FLAG-PHF2 was transfected into 3T3-L1 adipocytes. Cells were harvested and immunoprecipitated with anti-FLAG antibody and detected with anti-CEBPA antibody or anti-FLAG antibody. *C*: 3T3-L1 cells were fixed in formaldehyde on day 4 after differentiation, after which chromatin samples were subjected to ChIP analysis with indicated antibodies and amplified with primers toward indicated loci (n = 3). *D* and *E*: 3T3-L1 cells stably transfected with pSuper-retro-shLacZ or pSuper-retro-shPHF2 were differentiated into adipocytes and subjected to ChIP analysis with anti-CEBPA (*D*) or anti-H3K9me2 antibody (*E*), with primers toward the indicated loci (n = 3). *$P < 0.05$; **$P < 0.01$ compared with control. NC, negative control region.

a role as a coactivator, positively regulating adipogenic gene expression with CEBPA through H3K9me2 demethylation near CEBPA-binding regions.

DISCUSSION

To investigate the role of PHF2 in vivo, we generated *Phf2* knockout mice. *Phf2* knockout mice showed partial neonatal death, growth retardation, and reduced body weight. Reduced body weight seems to be mainly related to growth retardation and reduced lean mass in the knockout mice rather than reduced WAT mass because the body weight of *Phf2* knockout mice is still significantly lower than that of wild type at 8 weeks of age (Fig. 2*E*) when the weight of WAT is not different between *Phf2* knockout and wild type (Supplementary Fig. 1). The reason for this phenotype is not clear. PHF2 has been reported to be highly expressed in the neural tube and dorsal root ganglia (22), and *Phf2* represents a candidate gene for hereditary sensory neuropathy type I (HSN1) (23). In fact, the brain weights of *Phf2* knockout mice were larger than wild-type littermates. Taken together, we speculate that *Phf2* knockout mice may exhibit partial neonatal death attributable to defects in the central nervous system. Conditional deletion mutants using brain-specific Cre mice would clarify the precise roles of PHF2 in brain development.

On the other hand, subsequent study revealed that PHF2 plays an important role in adipogenesis. *Phf2* knockout mice produced lipoatrophy in which adipocytes were decreased in size and number. It seemed to be limited to a young age; for example, in *Klf5* knockout mice, atrophic changes in adipose tissue were abolished until 4 weeks of age (20). Although the reduced WAT phenotype in *Phf2* knockout mice disappeared after the mice reached 8 weeks of age and *Phf2* was systemically knocked out in these mice, this phenotype should be the result of a cell-autonomous mechanism because conditional knockout of *Phf2* in primary SVCs obtained from $Phf2^{fl/fl}$;*Cre-ERT* mice resulted in impaired adipogenesis. Moreover, PHF2 interacts with CEBPA, one of the master adipogenic regulators, and is recruited to CEBPRE. In addition, the lipoatrophic changes in *Phf2* knockout mice were stronger in epididymal and subcutaneous WAT than in mesenteric WAT, suggesting that PHF2 may be a possible candidate factor that determines regional variations in adipogenesis reported previously (24). Although adipose tissue is well known to be involved in glucose homeostasis, there was no significant change in glucose metabolism in *Phf2* knockout mice (Supplementary Fig. 3). There are two possible reasons for this result. First, 5 weeks of age is too young to develop insulin resistance, and second, only slight lipoatrophic change was observed in mesenteric WAT, the mass of which is strongly correlated with insulin resistance. It is meaningful to evaluate glucose metabolism of *Phf2* knockout adult mice under the treatment of a high-fat diet to clarify whether PHF2 plays a role in diabetes.

It is well known that factors that increase cAMP, such as isobutylmethylxanthine, strongly accelerate adipogenesis

(25). Elevation of cAMP is known to lead to suppression of Wnt10b (26) and Sp1 (27), induction of C/EBPβ (28), and production of PPARγ ligands (29). Moreover, cAMP signaling is mediated by two major pathways, PKA and Epac (exchange proteins directly activated by cAMP), that synergistically induce adipogenesis (30). However, it is not fully understood how PKA stimulates adipogenesis. PHF2 seems to be one possible candidate because it is reportedly activated through phosphorylation by PKA (5), and the current study shows that PHF2 stimulates adipogenesis. It seems that *Phf2* was not transcriptionally regulated during adipogenesis (Supplementary Fig. 4). However, PHF2 might be activated by PKA-mediated phosphorylation by a cAMP inducer in the adipogenic differentiation cocktail.

On the other hand, the weight reduction of BAT was not observed in *Phf2* knockout mice, although PKA and CEBPA were also reported to be necessary for the development of BAT (31). Recently, it was reported that brown adipocytes were differentiated from Myf5-positive precursor cells, which are more closely related to myoblasts rather than to the white preadipocytes (32). Thus, PHF2 may play a role in white preadipocytes but not in brown preadipocytes or myoblasts because the histone demethylases seem to be involved in differentiation in specific cell types.

PHF2 reportedly interacts with ARID5B, which is necessary for the coactivator function of PHF2 (5). Because phenotypes of systemic *Arid5b* knockout animals have already been reported (33–35), it is worth comparing the phenotypes between *Arid5b* knockout and *Phf2* knockout mice. Of note, most *Arid5b* knockout mice die within 24 h of birth, but some pups survive (33). The surviving *Arid5b* knockout animals show dramatically reduced body weight in neonates and adults. The WAT of *Arid5b* knockout mice weighed less than controls because of a reduction in the amount of lipid per cell. Because the phenotype of *Arid5b* knockout mice is close to that of *Phf2* knockout mice, it is likely that PHF2 and ARID5B work together in multiple organs, including adipose tissue.

Transcriptional control of the adipocyte lineage has been studied extensively (21,36). However, little is known about the role of histone demethylases during adipogenesis, even though several studies have clarified the roles of histone deacetylase HDAC1 (37,38) and HDAC3 (39) and histone demethylase LSD1 (40) in adipogenesis. In the current study, we found that histone demethylase PHF2 plays an important role in adipogenesis in vivo. Notably, several studies reported the role of histone demethylation in cell differentiation; for example, LSD1 controls pituitary terminal cell-type differentiation (6), JMJD3, an H3K27me3 demethylase, potentiates epidermal differentiation (41); and JMJD1A, an H3K9 demethylase, potentiates smooth muscle cell differentiation (42). In general, histone demethylases may play roles in cell differentiation in specific cell types. We suggest that PHF2 may be a significant histone demethylase in adipocytogenesis.

Adipose tissue plays an essential role in energy homeostasis. In mammals, WAT stores excess energy as triglycerides from fatty acids imported from circulating lipoproteins. Moreover, recent studies established adipose tissue as an active endocrine organ that secretes various humoral factors called adipokines that work in various physiological pathways, such as feeding, insulin resistance, inflammation, and atherogenesis (43). Thus, clarifications of precise molecular mechanisms that control adipose tissue development should improve our understanding of the pathogenesis and pathophysiology of the metabolic syndrome, diabetes, and other metabolism-related diseases. In this study, PHF2 appears to be a novel molecule that controls adipogenesis in vivo. Modulation of enzymatic activities has been a good target of small molecules. In fact, some drugs that can modulate the activities of histone-modifying enzymes have been developed for clinical use (44–46). Thus, pharmacological modulation of the histone demethylase activity of PHF2 may be a new target in the treatment of human lipodystrophies or adipocyte hyperplasia in diet-induced obesity.

ACKNOWLEDGMENTS

This work was supported by Grants-in-Aid 22790848 from the Ministry of Education, Culture, Sports, Science and Technology (to Y.O.) and a grant for specially promoted research from the Japan Society for the Promotion of Science (to S.K.).

No potential conflicts of interest relevant to this article were reported.

The funder played no role in the conduct of the study, collection of data, management of the study, analysis of data, interpretation of data, or preparation of the manuscript.

Y.O. wrote the manuscript and analyzed data. F.O., T.M., I.T., S.K., and Y.I. designed the experiments. F.O. and Y.I. reviewed and edited the manuscript. K.I. and J.K. performed the microarray analyses. Y.I. is the guarantor of this work and, as such, had full access to all the data in the study and takes responsibility for the integrity of the data and the accuracy of the data analysis.

The authors thank Yoko Yamamoto, Kazuki Inoue, and Erina Inoue, Laboratory of Epigenetic Skeletal Diseases, Institute of Molecular and Cellular Biosciences, The University of Tokyo, Japan, for technical support in the generation of knockout mice.

REFERENCES

1. Jenuwein T, Allis CD. Translating the histone code. Science 2001;293:1074–1080
2. Klose RJ, Kallin EM, Zhang Y. JmjC-domain-containing proteins and histone demethylation. Nat Rev Genet 2006;7:715–727
3. Shi Y. Histone lysine demethylases: emerging roles in development, physiology and disease. Nat Rev Genet 2007;8:829–833
4. Agger K, Christensen J, Cloos PA, Helin K. The emerging functions of histone demethylases. Curr Opin Genet Dev 2008;18:159–168
5. Baba A, Ohtake F, Okuno Y, et al. PKA-dependent regulation of the histone lysine demethylase complex PHF2-ARID5B. Nat Cell Biol 2011;13:668–675
6. Wang J, Scully K, Zhu X, et al. Opposing LSD1 complexes function in developmental gene activation and repression programmes. Nature 2007;446:882–887
7. Okada Y, Scott G, Ray MK, Mishina Y, Zhang Y. Histone demethylase JHDM2A is critical for *Tnp1* and *Prm1* transcription and spermatogenesis. Nature 2007;450:119–123
8. Tateishi K, Okada Y, Kallin EM, Zhang Y. Role of Jhdm2a in regulating metabolic gene expression and obesity resistance. Nature 2009;458:757–761
9. Qi HH, Sarkissian M, Hu GQ, et al. Histone H4K20/H3K9 demethylase PHF8 regulates zebrafish brain and craniofacial development. Nature 2010;466:503–507
10. Tsukada Y, Ishitani T, Nakayama KI. KDM7 is a dual demethylase for histone H3 Lys 9 and Lys 27 and functions in brain development. Genes Dev 2010;24:432–437
11. Wen H, Li J, Song T, et al. Recognition of histone H3K4 trimethylation by the plant homeodomain of PHF2 modulates histone demethylation. J Biol Chem 2010;285:9322–9326
12. Lee EC, Yu D, Martinez de Velasco J, et al. A highly efficient *Escherichia coli*-based chromosome engineering system adapted for recombinogenic targeting and subcloning of BAC DNA. Genomics 2001;73:56–65

13. Dupé V, Davenne M, Brocard J, et al. In vivo functional analysis of the Hoxa-1 3′ retinoic acid response element (3′RARE). Development 1997; 124:399–410
14. Ruzankina Y, Pinzon-Guzman C, Asare A, et al. Deletion of the developmentally essential gene *ATR* in adult mice leads to age-related phenotypes and stem cell loss. Cell Stem Cell 2007;1:113–126
15. Iwaki M, Matsuda M, Maeda N, et al. Induction of adiponectin, a fat-derived antidiabetic and antiatherogenic factor, by nuclear receptors. Diabetes 2003;52:1655–1663
16. Ohtake F, Baba A, Takada I, et al. Dioxin receptor is a ligand-dependent E3 ubiquitin ligase. Nature 2007;446:562–566
17. Kanno J, Aisaki K, Igarashi K, et al. "Per cell" normalization method for mRNA measurement by quantitative PCR and microarrays. BMC Genomics 2006;7:64
18. Mersmann HJ, MacNeil MD. Variables in estimation of adipocyte size and number with a particle counter. J Anim Sci 1986;62:980–991
19. Ramírez-Zacarías JL, Castro-Muñozledo F, Kuri-Harcuch W. Quantitation of adipose conversion and triglycerides by staining intracytoplasmic lipids with Oil red O. Histochemistry 1992;97:493–497
20. Oishi Y, Manabe I, Tobe K, et al. Krüppel-like transcription factor KLF5 is a key regulator of adipocyte differentiation. Cell Metab 2005;1:27–39
21. Farmer SR. Transcriptional control of adipocyte formation. Cell Metab 2006;4:263–273
22. Hasenpusch-Theil K, Chadwick BP, Theil T, Heath SK, Wilkinson DG, Frischauf AM. PHF2, a novel PHD finger gene located on human chromosome 9q22. Mamm Genome 1999;10:294–298
23. Nicholson GA, Dawkins JL, Blair IP, et al. The gene for hereditary sensory neuropathy type I (HSN-I) maps to chromosome 9q22.1-q22.3. Nat Genet 1996;13:101–104
24. Tchkonia T, Giorgadze N, Pirtskhalava T, et al. Fat depot origin affects adipogenesis in primary cultured and cloned human preadipocytes. Am J Physiol Regul Integr Comp Physiol 2002;282:R1286–R1296
25. Yarwood SJ, Anderson NG, Kilgour E. Cyclic AMP modulates adipogenesis in 3T3-F442A cells. Biochem Soc Trans 1995;23:175S
26. Bennett CN, Ross SE, Longo KA, et al. Regulation of Wnt signaling during adipogenesis. J Biol Chem 2002;277:30998–31004
27. Tang QQ, Jiang MS, Lane MD. Repressive effect of Sp1 on the C/EBPalpha gene promoter: role in adipocyte differentiation. Mol Cell Biol 1999;19: 4855–4865
28. Yeh WC, Cao Z, Classon M, McKnight SL. Cascade regulation of terminal adipocyte differentiation by three members of the C/EBP family of leucine zipper proteins. Genes Dev 1995;9:168–181
29. Tzameli I, Fang H, Ollero M, et al. Regulated production of a peroxisome proliferator-activated receptor-gamma ligand during an early phase of adipocyte differentiation in 3T3-L1 adipocytes. J Biol Chem 2004;279: 36093–36102
30. Petersen RK, Madsen L, Pedersen LM, et al. Cyclic AMP (cAMP)-mediated stimulation of adipocyte differentiation requires the synergistic action of Epac- and cAMP-dependent protein kinase-dependent processes. Mol Cell Biol 2008;28:3804–3816
31. Wang ND, Finegold MJ, Bradley A, et al. Impaired energy homeostasis in C/EBP alpha knockout mice. Science 1995;269:1108–1112
32. Seale P, Bjork B, Yang W, et al. PRDM16 controls a brown fat/skeletal muscle switch. Nature 2008;454:961–967
33. Whitson RH, Tsark W, Huang TH, Itakura K. Neonatal mortality and leanness in mice lacking the ARID transcription factor Mrf-2. Biochem Biophys Res Commun 2003;312:997–1004
34. Lahoud MH, Ristevski S, Venter DJ, et al. Gene targeting of Desrt, a novel ARID class DNA-binding protein, causes growth retardation and abnormal development of reproductive organs. Genome Res 2001;11:1327–1334
35. Schmahl J, Raymond CS, Soriano P. PDGF signaling specificity is mediated through multiple immediate early genes. Nat Genet 2007;39:52–60
36. MacDougald OA, Lane MD. Transcriptional regulation of gene expression during adipocyte differentiation. Annu Rev Biochem 1995;64:345–373
37. Wiper-Bergeron N, Wu D, Pope L, Schild-Poulter C, Haché RJ. Stimulation of preadipocyte differentiation by steroid through targeting of an HDAC1 complex. EMBO J 2003;22:2135–2145
38. Yoo EJ, Chung JJ, Choe SS, Kim KH, Kim JB. Down-regulation of histone deacetylases stimulates adipocyte differentiation. J Biol Chem 2006;281: 6608–6615
39. Fajas L, Egler V, Reiter R, et al. The retinoblastoma-histone deacetylase 3 complex inhibits PPARgamma and adipocyte differentiation. Dev Cell 2002;3:903–910
40. Musri MM, Carmona MC, Hanzu FA, Kaliman P, Gomis R, Párrizas M. Histone demethylase LSD1 regulates adipogenesis. J Biol Chem 2010;285: 30034–30041
41. Sen GL, Webster DE, Barragan DI, Chang HY, Khavari PA. Control of differentiation in a self-renewing mammalian tissue by the histone demethylase JMJD3. Genes Dev 2008;22:1865–1870
42. Lockman K, Taylor JM, Mack CP. The histone demethylase, Jmjd1a, interacts with the myocardin factors to regulate SMC differentiation marker gene expression. Circ Res 2007;101:e115–e123
43. Flier JS. Obesity wars: molecular progress confronts an expanding epidemic. Cell 2004;116:337–350
44. McCabe MT, Ott HM, Ganji G, et al. EZH2 inhibition as a therapeutic strategy for lymphoma with EZH2-activating mutations [letter to the editor online], 2012. Available from http://www.nature.com/nature/journal/vaop/ncurrent/full/nature11606.html. Accessed 2 November 2012
45. Song SH, Han SW, Bang YJ. Epigenetic-based therapies in cancer: progress to date. Drugs 2011;71:2391–2403
46. Tan J, Cang S, Ma Y, Petrillo RL, Liu D. Novel histone deacetylase inhibitors in clinical trials as anti-cancer agents. J Hematol Oncol 2010;3:5

OPEN ACCESS Freely available online

PLoS one

Minichromosome Maintenance 2 Bound with Retroviral Gp70 Is Localized to Cytoplasm and Enhances DNA-Damage-Induced Apoptosis

Shinya Abe[1], Morito Kurata[1], Shiho Suzuki[1], Kouhei Yamamoto[1], Ken-ichi Aisaki[2], Jun Kanno[2], Masanobu Kitagawa[1]*

1 Department of Comprehensive Pathology, Graduate School of Medical and Dental Sciences, Tokyo Medical and Dental University, Tokyo, Japan, **2** Division of Cellular and Molecular Toxicology, National Institute of Health Sciences, Tokyo, Japan

Abstract

The interaction of viral proteins with host-cellular proteins elicits the activation of cellular signal transduction pathways and possibly leads to viral pathogenesis as well as cellular biological events. Apoptotic signals induced by DNA-damage are remarkably up-regulated by Friend leukemia virus (FLV) exclusively in C3H hosts; however, the mechanisms underlying the apoptosis enhancement and host-specificity are unknown. Here, we show that C3H mouse-derived hematopoietic cells originally express higher levels of the minichromosome maintenance (MCM) 2 protein than BALB/c- or C57BL/6-deriverd cells, and undergo more frequent apoptosis following doxorubicin-induced DNA-damage in the presence of the FLV envelope protein gp70. Dual transfection with *gp70/Mcm2* reproduced doxorubicin-induced apoptosis even in BALB/c-derived 3T3 cells. Immunoprecipitation assays using various deletion mutants of MCM2 revealed that gp70 bound to the nuclear localization signal (NLS) 1 (amino acids 18–24) of MCM2, interfered with the function of NLS2 (amino acids 132–152), and suppressed the normal nuclear-import of MCM2. Cytoplasmic MCM2 reduced the activity of protein phosphatase 2A (PP2A) leading to the subsequent hyperphosphorylation of DNA-dependent protein kinase (DNA-PK). Phosphorylated DNA-PK exhibited elevated kinase activity to phosphorylate P53, thereby up-regulating *p53*-dependent apoptosis. An apoptosis-enhancing domain was identified in the C-terminal portion (amino acids 703–904) of MCM2. Furthermore, simultaneous treatment with FLV and doxorubicin extended the survival of SCID mice bearing 8047 leukemia cells expressing high levels of MCM2. Thus, depending on its subcellular localization, MCM2 plays different roles. It participates in DNA replication in the nucleus as shown previously, and enhances apoptosis in the cytoplasm.

Citation: Abe S, Kurata M, Suzuki S, Yamamoto K, Aisaki K-i, et al. (2012) Minichromosome Maintenance 2 Bound with Retroviral Gp70 Is Localized to Cytoplasm and Enhances DNA-Damage-Induced Apoptosis. PLoS ONE 7(6): e40129. doi:10.1371/journal.pone.0040129

Editor: Junji Yodoi, Institute for Virus Research, Laboratory of Infection and Prevention, Japan

Received March 2, 2012; **Accepted** June 1, 2012; **Published** June 29, 2012

Funding: This work was supported by a grant-in-aid (21590432) from the Ministry of Education, Culture, Sports, Science, and Technology of Japan and by Health Sciences Research Grant H18-Kagaku-001 from the Ministry of Health, Labour and Welfare of Japan. The funders had no role in study design, data collection and analysis, decision to publish, or preparation of the manuscript.

Competing Interests: The authors have declared that no competing interests exist.

* E-mail: masa.pth2@tmd.ac.jp

Introduction

Because ionizing irradiation (IR) and chemical agents such as doxorubicin exhibit cell-killing activity by inducing double-strand breaks (DSBs) and *p53*-dependent apoptosis, they have been considered therapeutic tools against malignant tumors [1–5]. To protect normal cells from injury, tumor cell-specific induction of apoptosis would be one of the most important properties of anti-tumor therapeutics [6,7]. To regulate the *p53*-dependent apoptosis caused by DNA-damage, an understanding of upstream activators or regulators of P53 would be vital. These pathways partly involve the phosphatidylinositol 3-kinase (PI3K)-related protein kinase (PIKK) family of enzymes [8], including ataxia telangiectasia (ATM), ATM and Rad3-related (ATR), and DNA-dependent protein kinase (DNA-PK) [9–13].

Viral infections are known to modify cellular processes related to DNA-damage responses or DNA synthesis [14–16]. We have previously shown that Friend leukemia virus (FLV) infection markedly enhances the IR-induced apoptosis of hematopoietic cells in C3H mice via P53, ATM, and DNA-PK [17]. Mice infected with FLV and then treated with a low dose of total body irradiation (TBI) exhibit severe anemia. However, *p53* knockout mice, *Atm* knockout mice, and DNA-PK-deficient SCID mice with a C3H background do not exhibit this phenotype. A comparison of the apoptotic signals after FLV infection, TBI, or FLV+TBI treatment of these mice revealed that ATM is necessary for the general signal transduction of TBI-induced apoptosis [18], while DNA-PK plays a specific role in enhancing *p53*-dependent apoptosis following FLV infection [19,20].

The enhancement of *p53*-dependent apoptosis occurs almost exclusively in the C3H strain of mice [21]. In relation to this host-specific apoptosis-enhancement, we have previously demonstrated that the FLV-derived envelope protein gp70 enhances cellular apoptotic signaling in association with host-specific overexpressed proteins, including the minichromosome maintenance (MCM) 2 protein, resulting in the activation of DNA-PK, which phosphorylates P53 [22]. MCM2 is one of a set of 6 proteins (MCM complex; MCM2-7) that play essential roles in DNA replication [23]. The MCM complex associates with the origins of DNA

replication to form part of the pre-replicative complex (preRC) [24]. Activation of the MCM complex by cyclin-dependent kinases leads to the initiation of DNA synthesis and MCM proteins also act as a replicative helicase to unwind DNA at replication forks during DNA synthesis [25,26]. The MCM complex contains a nuclear localization signal (NLS) and a nuclear export signal (NES) [27]. The NLS is split between MCM2 and MCM3 and the NES is located in MCM3 adjacent to the NLS sequence. The transport of all MCM proteins is interdependent, suggesting that nuclear import requires the formation of the hexameric complex, which would result in the assembly of a complete NLS [28,29]. MCM proteins are expressed in cycling cells but are down-regulated and dissociated from the chromatin in quiescent cells [30]. Thus, detection of MCM proteins has emerged as a method for evaluating the proliferative state and growth fraction in dynamic cell populations. Indeed, elevated expression of several members of the MCM complex has been reported in various malignant tumors [31,32]. Furthermore, studies with human samples have indicated the utility of MCM2 as a proliferation marker, and a high level of MCM2 expression in malignant tumors has been associated with several clinicopathological parameters, such as advanced tumor grade, advanced stage, and poor prognosis [33–36]. Thus, MCM2 usually acts to support cellular proliferation. However, as described above, MCM2 enhances TBI-induced apoptosis in the presence of gp70. To determine importance of such contradictory functions of the MCM2 protein in the regulation of cellular dynamics, the molecular mechanisms underlying MCM2-induced apoptosis and MCM2-gp70 interaction need to be elucidated. An understanding of the overall functions of MCM2 would enable the molecular targeting of specific functions possibly to regulate cellular proliferation/apoptosis in a cell type-specific manner and develop a novel strategy to control tumor cell growth.

Results

Doxorubicin-induced Apoptosis of FLV-infected Cells Correlates with High Levels of *Mcm2 in Vivo*

In previous studies, TBI caused prominent apoptosis in the bone marrow cells of FLV-infected C3H mice, but not FLV-infected BALB/c and C57BL/6 mice [17]. From a therapeutic perspective, systemic distribution of the effects of DNA-damage would be more easily achieved by chemical agents than IR. Therefore, to determine whether DNA-damaging agents enhanced apoptosis to similar extents in FLV-infected mice of different strains, uninfected or FLV-infected BALB/c, C57BL/6, and C3H mice were intraperitoneally administered with a low dose of doxorubicin or PBS, and the apoptotic cell ratio was measured in the bone marrow and spleen. In FLV-infected BALB/c and C57BL/6 mice, the apoptotic cell ratios after treatment with doxorubicin were similar to the ratios in uninfected mice (Figure 1A, B). On the other hand, FLV-infected doxorubicin-treated C3H mice exhibited significantly higher ratios with uninfected mice (Figure 1C). Thus, we could generalize as to the effects of DNA-damage by IR and chemical agents on the enhancement of apoptosis by FLV-infection in hematopoietic organs.

Next, we examined the expression of *Mcm2* mRNA in the bone marrow and spleen of uninfected and FLV-infected BALB/c, C57BL/6, and C3H mice. *Mcm2* levels were significantly higher in the bone marrow cells of C3H mice than in BALB/c and C57BL/6 mice (Figure 1D). Spleen *Mcm2* levels were also higher in C3H mice than in BALB/c and C57BL/6 mice. Furthermore, in C3H mice, the spleen *Mcm2* levels were elevated by FLV-infection (Figure 1E). Similar trends were observed across all the inbred strains tested. These results suggest that doxorubicin treatment induces significant apoptosis in FLV-infected C3H mice in association with higher levels of *Mcm2*. Moreover, we performed a comparative GeneChip analysis using RNA isolates from mouse spleen and identified several genes that exhibited various expression patterns in the different mouse strains (Figure 1F-L). *Mcm2* expression was higher in C3H mice than in C57BL/6 mice, and *Mcm2* expression was elevated by FLV-infection (Figure 1G). Genes that exhibited expression patterns similar to that of *Mcm2* are listed in Table S1.

Dual Transfection with *Mcm2/gp70* Enhances DNA-damage-induced Apoptosis in BALB/c-derived 3T3 Cells

To investigate whether apoptosis enhancement was related to the high levels of *Mcm2* in FLV-infected cells, we analyzed doxorubicin-induced apoptosis sensitivity in *Mcm2* and/or *gp70*-transfected 3T3 cells. First, the expression of *Mcm2* was analyzed in each mouse cell line. BALB/c-derived 3T3 cells and primary cultured BALB/c-fibroblasts expressed low levels of *Mcm2* compared to C3H-derived 8047 cells, 32D cells and primary cultured C3H-fibroblasts (Figure 2A).

Next, the viability and apoptotic cell ratios of 3T3 cells were evaluated after doxorubicin treatment. *Gp70* plus *Mcm2*-transfected 3T3 cells exhibited a significant decrease in viability and an increase in apoptotic cell ratio compared to control cells, whereas cells transfected with *gp70* or *Mcm2* exhibited no significant change in viability and apoptotic cell ratio (Figure 2B, C). Gp70 and/or MCM2 protein levels following *gp70*- and/or *Mcm2*-transfection were similar in all the experimental groups (Figure 2D). Next, we knocked down the expression of *Mcm2* in BaF3 and 32D cells using siRNA. The 32D cell line, with a high level of endogenous gp70 expression, was established from FLV-infected C3H mouse bone marrow [37] (Figure 2E). *Mcm2* knockdown significantly reduced *Mcm2* mRNA expression and apoptotic cell ratio of 32D cells treated with doxorubicin in contrast to the non-remarkable change in the apoptotic cell ratio of BaF3 cells (Figure 2F). These results suggest that the host-specific enhancement of DNA-damage-induced apoptosis is associated with the higher level of *Mcm2* expression in C3H-derived cells.

Gp70 Directly Binds to the N-terminal Portion of MCM2

To examine the molecular interactions between MCM2 and gp70, immunoprecipitation experiments were performed. We generated plasmids encoding HA-tagged full-length MCM2 (MCM2-FL) and various deletion mutants: MCM2-ΔC, MCM2-ΔN, MCM2-N and MCM2-C (Figure 3A). Each of these plasmids was transfected into 3T3 cells along with *FLAG*-tagged *gp70*. Irrespective of doxorubicin treatment, gp70 interacted with MCM2-FL, MCM2-ΔC, and MCM2-N, but not with MCM2-ΔN or MCM2-C (Figure 3B, C). These results indicate that gp70 associates with the N-terminal portion of MCM2. Gp70 binding inhibited the formation of the MCM complex (Figure S1). As shown in Figure 3B and 3C, the size of MCM2-N was larger than the expected size. Generally, phosphorylated proteins are sometimes larger than their unphosphorylated counterparts [38,39]. Indeed, the N-terminal portion of MCM2 possesses many phosphorylation sites [40]. Therefore, the apparent molecular weight of MCM2-N may be higher than expected. Further, MCM2-C does not have as many phosphorylation sites [40]. As a result, MCM2-N may appear larger than MCM2-C.

We also generated plasmids encoding a FLAG-tagged gp70 deletion mutant (Figure S2A) and performed a similar pull-down assay after co-transfection with HA-tagged *Mcm2*-FL. MCM2 bound to the middle portion of gp70 (Figure S2B, C) and enhanced apoptosis in response to doxorubicin (Figure S2D, E).

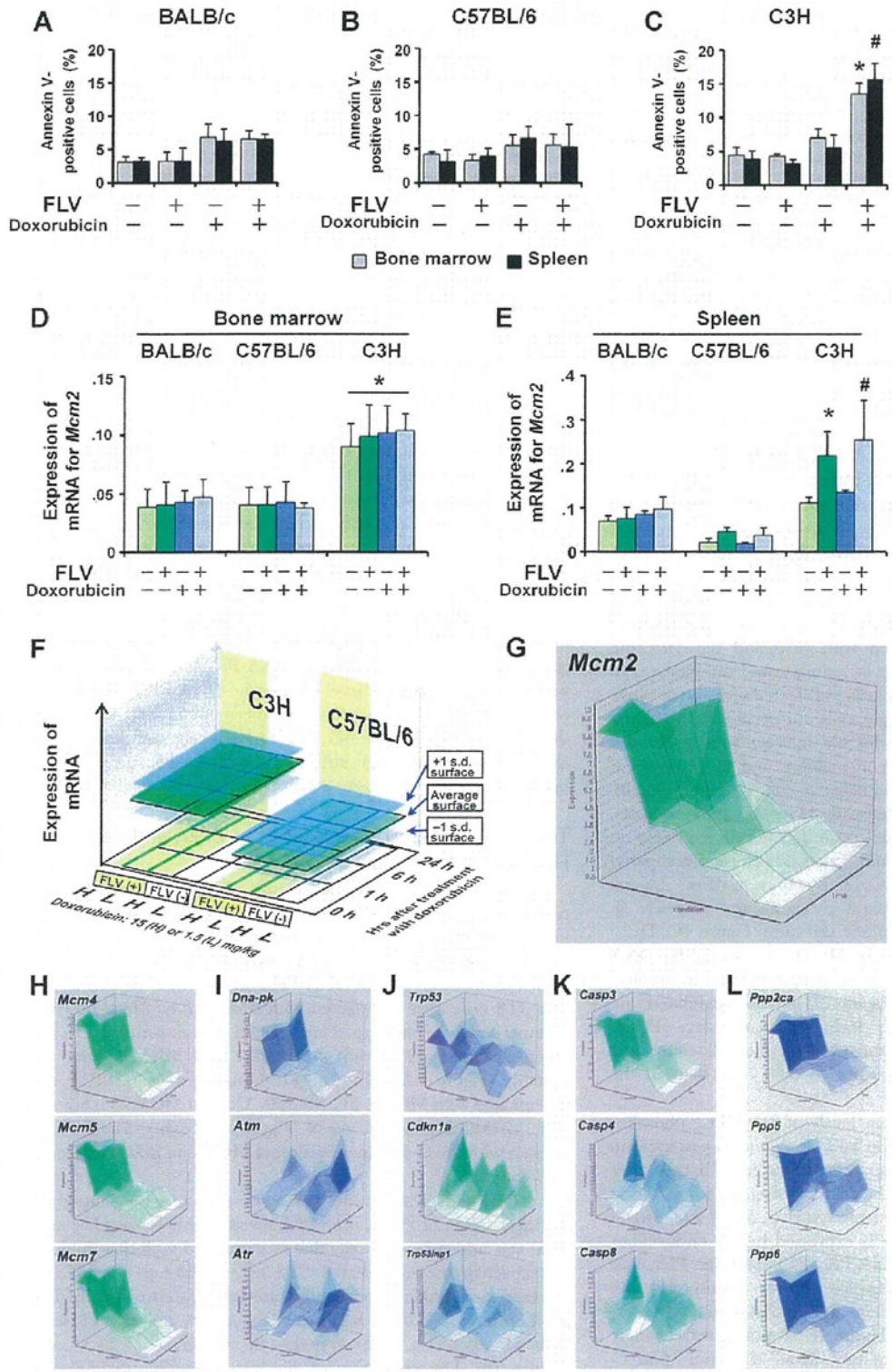

Figure 1. ***In vivo*** **assessment of doxorubicin-induced apoptosis and the associated changes in mRNA expression in FLV-infected mice.** Uninfected or FLV-infected BALB/c (A), C57BL/6 (B), and C3H (C) mice were intraperitoneally (i.p.) administrated with 1.5 mg/kg of doxorubicin or PBS, and the apoptotic cell ratios in the bone marrow (gray bars) and spleen cells (black bars) were determined 24 h later with annexin V-staining. Note the significant increase in the proportion of annexin V-positive cells in the bone marrow and spleen of FLV-infected C3H mice after the doxorubicin treatment compared to that in the bone marrow and spleen cells of uninfected mice "FLV (−), Doxorubicin (−)" (*$p<0.01$ and $^{\#}p<0.01$).

Data represent the mean and 95% confidence intervals (CI) of 3 independent experiments. (D) Quantitative RT-PCR analysis of *Mcm2* mRNA expression in the bone marrow of uninfected and FLV-infected BALB/c, C57BL/6, and C3H mice. The bone marrow cells of the C3H strain exhibit higher levels of *Mcm2* in all groups compared to the corresponding groups of BALB/c and C57BL/6 mice ($^{*}p<0.01$, for each group). (E) Quantitative RT-PCR analysis of *Mcm2* mRNA expression in the spleen of uninfected and FLV-infected BALB/c, C57BL/6, and C3H mice. Spleen *Mcm2* expression is higher in the "FLV (+), Doxorubicin (−)" and "FLV (+), Doxorubicin (+)" C3H mice than in the corresponding groups of BALB/c and C57BL/6 mice ($^{*}p<0.01$ and $^{\#}p<0.01$, respectively). In C3H mice, FLV-infection induces higher levels of *Mcm2* expression compared to the expression in uninfected mice. Data represent the mean and 95% CI from 5 mice in each group and are representative of 2 independent experiments. The GeneChip data for *Mcm*-associated and apoptosis-associated genes were analyzed using the Percellome method. Forty-eight male C57BL/6 and C3H mice were divided into 16 groups of 3 mice each. Uninfected or FLV-infected C57BL/6 and C3H mice were administered (i.p.) with 15 mg/kg (high dose) or 1.5 mg/kg (low dose) of doxorubicin, and the spleen was sampled 0, 1, 6, and 24 h after administration. The spleen transcriptome was measured using the Affymetrix Mouse 430-2 GeneChip. (F) The Percellome data were plotted on 3-dimensional graphs for average, +1 SD, and −1 SD surfaces as demonstrated in the left schema. The scale of expression (vertical axis) is the copy number per cell. The x-axis of the 3-dimensional graph shows the experimental groups, including the C3H and C57BL/6 mice with doxorubicin treatment (high and low doses) with or without FLV-infection. The y-axis shows the time course (0, 1, 6, and 24 h) after treatment with doxorubicin and the z-axis (vertical) indicates the intensity of mRNA expression of each gene. The data of each point are connected to form a surface illustration. The expression patterns of genes are compared using the surface images. (G) The *Mcm2* expression pattern is shown in the upper right box. Of the lower columns, the first column (H) shows the data for the genes of representative *Mcm* family members, the second column (I), PI3K members, the third column (J), p53-associated genes, the fourth column (K), caspase members and fifth column (L), protein phosphatase members (PPs). *Mcm* family members, *Dna-pk*, *caspase-3* (*Casp3*), *Ppp2ac*, and *Ppp6* exhibit gene expression patterns similar to that of *Mcm2*.

doi:10.1371/journal.pone.0040129.g001

The C-terminal Portion of MCM2 is Essential for the Enhancement of Doxorubicin-induced Apoptosis

Next, to identify the functional domain of MCM2 essential for apoptosis enhancement following DNA-damage, a functional analysis was performed using MCM2 deletion mutants. First, *Mcm2-FL* or the deletion mutant were introduced into 3T3 cells with or without *gp70*. After the transfection, 3T3 cells were treated with doxorubicin, and cell viability and apoptotic cell ratio were measured. 3T3 cells, transfected with *gp70* and the *Mcm2-FL* exhibited a significant decrease in viability and an increase in apoptotic cell ratio compared to cells transfected with the negative control (Figure 4A, B). Surprisingly, cells transfected with *gp70* and *Mcm2-ΔN-* or *Mcm2-C*, which did not interact with gp70, also exhibited a significant decrease in viability and an increase in apoptotic cell ratio relative to the negative control (Figure 4A, B). Among the cells singly transfected with *Mcm2-FL* or the mutants, *Mcm2-FL-*, *Mcm2-ΔC-*, and *Mcm2-N*-transfected cells exhibited no remarkable change in viability and apoptotic cell ratio compared to the negative control (Figure 4C, D). By contrast, *Mcm2-ΔN* and *Mcm2-C*-transfected cells exhibited a significant decrease in viability and an increase in apoptotic cell ratio (Figure 4C, D).

Previous studies have shown that MCM2 is essential for DNA replication [23,25], and its expression is up-regulated in proliferating cells [41]. *Mcm2*-transfected 3T3 cells exhibited no significant change in cell count during the early stage (Figure S3A, B). However, at a later-stage (96 h), the cell count was significantly higher in *Mcm2*-transfected 3T3 cells than in the control (Figure S3C, D).

We next examined the protein levels of DNA-PK, phospho-DNA-PK (pS2053), P53, phospho-P53, and cleaved caspase-3 in *Mcm2-FL-* or Mcm2 deletion mutant-transfected 3T3 cells after doxorubicin treatment. Among the cells transfected with *gp70* plus *Mcm2-FL-* or *gp70* plus mutant-transfected cells, *Mcm2-FL-*, *Mcm2-ΔN-*, and *Mcm2-C*-transfected cells expressed higher endogenous levels of DNA-PK, phospho-DNA-PK, P53, phospho-P53, and cleaved caspase-3 than the negative control (Figure 4E). By contrast, the levels of these proteins in *Mcm2-ΔC-* and *Mcm2-N*-transfected cells did not change (Figure 4E). Among the cells singly transfected with *Mcm2-FL* or a mutant, *Mcm2-ΔN-*, and *Mcm2-C*-transfected cells exhibited higher levels of DNA-PK, phospho-DNA-PK, P53, phospho-P53, and cleaved caspase-3 after doxorubicin treatment (Figure 4F). These results indicate that not only the binding of MCM2 with gp70 but also deletion of the N-terminal portion enhances DNA-damage-induced apoptosis via the activation of P53 by DNA-PK. Furthermore, MCM2 lacking the C-terminal portion did not induce apoptosis even with *gp70* co-expression indicating that the C-terminal portion of MCM2 was essential for the enhancement of DNA-damage-induced apoptosis.

DNA-PK is robustly activated by auto-phosphorylation at Ser 2056 (S2053 in mouse) in apoptotic cells [42], while phosphorylation at Thr 2609 is associated with non-homologous end joining [43]. Therefore, to examine whether DNA-PK was exclusively required for the enhancement of apoptosis, we inhibited DNA-PK activity using NU7026 in the presence (Figure 4G) or absence of *gp70* (Figure 4H). Inhibition of DNA-PK activity by NU7026 substantially reduced the level of phospho-DNA-PK (pS2053) and completely abolished apoptosis enhancement in cells expressing the *Mcm2 mutants* (Figure 4G, H). These results and knockdown experiments (Figure S4) indicate that DNA-PK activation is necessary for the enhancement of doxorubicin-induced apoptosis.

The Gp70-MCM2 Complex Binds to PP2A and Causes Hyperphosphorylation of DNA-PK

To determine the mechanism by which the gp70-MCM2 complex activated DNA-PK to enhance apoptosis, we sought to identify the upstream regulatory factors of DNA-PK. We focused on protein phosphatase 2A (PP2A), because this molecule has been shown to dephosphorylate DNA-PK and control its function [44–46]. 3T3 cells were transfected with *Mcm2-FL* or *Mcm2* deletion mutants with or without *gp70* and treated with doxorubicin. In the absence of *gp70*, PP2A did not interact with MCM2-FL or the mutants (Figure 5A, left). In *gp70*-transfected cells, PP2A co-precipitated with MCM2-FL, MCM2-ΔN, and MCM2-C, but not with MCM2-ΔC or MCM2-N (Figure 5A, right). Thus, PP2A interact with the C-terminal portion of MCM2 in *gp70*-transfected 3T3 cells.

To determine whether the enhanced apoptosis was caused by the inactivation of PP2A, the PP2A-specific inhibitor okadaic acid (OA) was added to 3T3 cells that were treated with doxorubicin. As expected, the OA-treated 3T3 cells exhibited a significant increase in apoptotic cell ratio compared to the control (Figure 5B). Furthermore, NU7026 treatment abrogated the doxorubicin-induced apoptosis enhancement in OA-treated 3T3 cells (Figure 5B). The expression of phospho-DNA-PK (pS2053) was upregulated in OA-treated 3T3 cells after doxorubicin treatment (Figure 5C). These results suggest that the gp70-MCM2 complex binds to and inhibits PP2A. Consequently, DNA-PK is hyperphosphorylated and doxorubicin-induced apoptosis is enhanced via the P53/cleaved caspase-3 pathway.

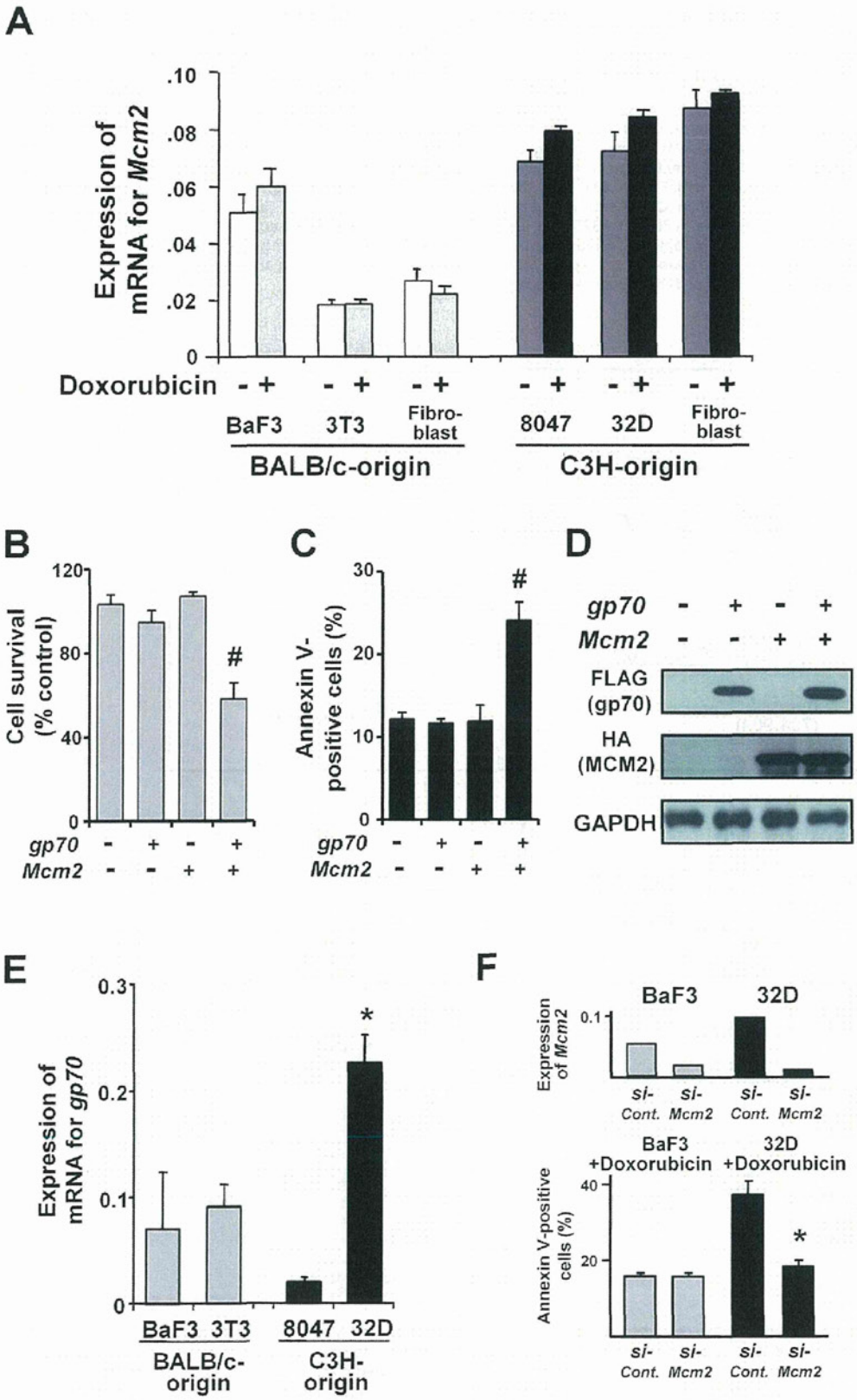
A
Expression of mRNA for Mcm2
.10
.08
.06
.04
.02
0
Doxorubicin - + - + - + - + - + - +
BaF3
3T3
Fibro-blast
8047
32D
Fibro-blast
BALB/c-origin
C3H-origin
B
Cell survival (% control)
120
80
40
0
#
gp70 - + - +
Mcm2 - - + +
C
Annexin V-positive cells (%)
30
20
10
0
#
gp70 - + - +
Mcm2 - - + +
D
gp70 - + - +
Mcm2 - - + +
FLAG (gp70)
HA (MCM2)
GAPDH
E
Expression of mRNA for gp70
0.3
0.2
0.1
0
*
BaF3 3T3
8047 32D
BALB/c-origin
C3H-origin
F
Expression of Mcm2
BaF3
32D
0.1
si-Cont. si-Mcm2 si-Cont. si-Mcm2
BaF3 +Doxorubicin
32D +Doxorubicin
Annexin V-positive cells (%)
40
20
*
si-Cont. si-Mcm2 si-Cont. si-Mcm2

Figure 2. Dual transfection of *gp70* and *Mcm2* enhances DNA-damage-induced apoptosis in 3T3 cells. (**A**) Quantitative RT-PCR analysis of *Mcm2* mRNA expression in untreated and doxorubicin-treated BALB/c-derived BaF3 and 3T3 cells, and primary cultured fibroblasts, and C3H-derived 8047 and 32D cells, and primary cultured fibroblasts. Data represent the mean and 95% CI of 3 independent experiments. (**B**) Cell survival (% of control) measured with the MTT assay in *gp70* and/or *Mcm2*-transfected 3T3 cells after treatment with doxorubicin for 24 h. Cell survival is significantly different between control cells "*gp70* (−), *Mcm2* (−)" and *gp70/Mcm2*-transfected cells "*gp70* (+), *Mcm2* (+)" (#$p<0.01$). Data represent the mean and 95% CI of 3 independent experiments. (**C**) Apoptotic cell ratios in *gp70* and/or *Mcm2*-transfected 3T3 cells were determined with annexin V-staining after treatment with 1 μM doxorubicin for 24 h. The ratios in the control cells "*gp70* (−), *Mcm2* (−)" and *gp70/Mcm2*-transfected cells "*gp70* (+), *Mcm2* (+)" are significantly different (#$p<0.01$). Data represent the mean and 95% CI of 3 independent experiments. (**D**) Western blot analysis of *gp70* and/or *Mcm2-FL*-transfected 3T3 cells after treatment with 1 μM of doxorubicin for 24 h. Gp70 and MCM2 protein levels are similar in all groups. (**E**) Expression of endogenous *gp70* mRNA in BaF3, 3T3, 8047, and 32D cells. *Gp70* mRNA expression (ng) was normalized to that of *GAPDH*. Note the significantly higher expression of *gp70* mRNA in 32D cells compared to that in the other cells (*$p<0.01$). Data show the mean and 95% CI of three independent experiments. (**F**) *Mcm2* knockdown in BaF3 and 32D cells using siRNA. Quantitative RT-PCR (upper) was performed to confirm *si-Mcm2*-induced reduction of *Mcm2* mRNA expression. Apoptotic cell ratios were determined with annexin V-staining after treatment with doxorubicin for 24 h (bottom). Note the significant decrease in the apoptotic cell ratio of 32D cells treated with *si-Mcm2*, compared to that of cells treated with *si-Control* (*$p<0.01$). Data show the mean and 95% CI of 3 independent experiments.
doi:10.1371/journal.pone.0040129.g002

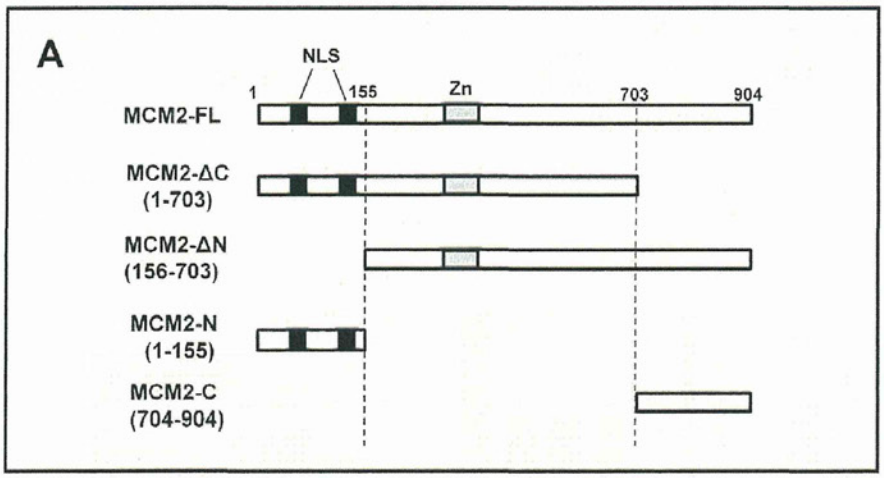

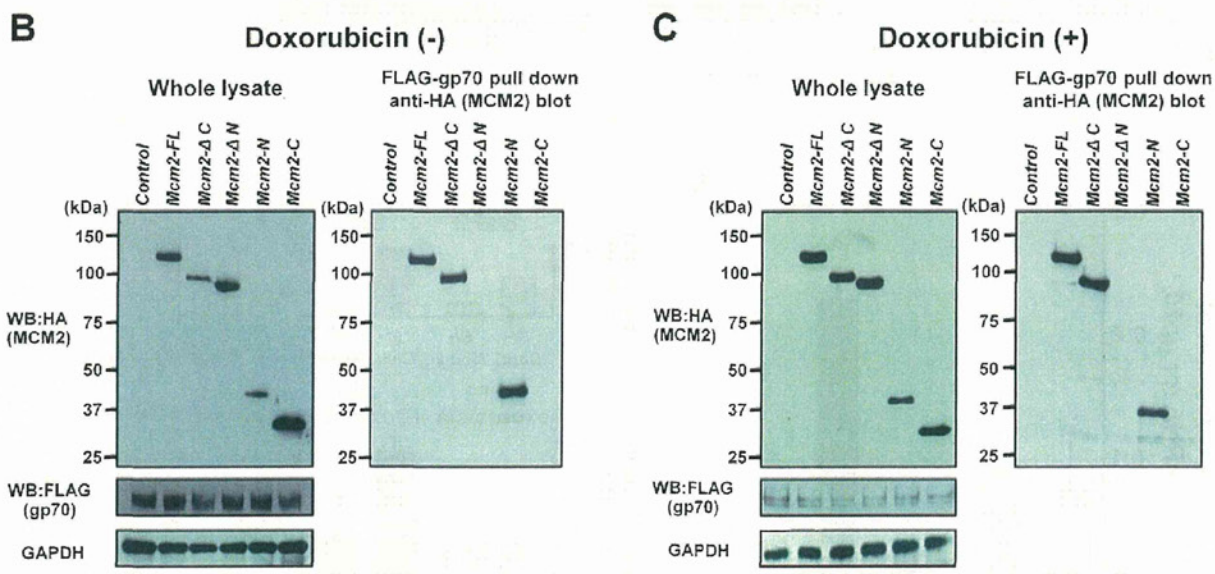

Figure 3. Direct interaction of MCM2 with gp70. (**A**) Schematic diagram of full-length MCM2 (MCM2-FL) and MCM2 deletion mutants, MCM2-ΔC (aa 1–703), MCM2-ΔN (aa 156–703), MCM2-N (aa 1–155) and MCM2-C (aa 704–904). The NLS domains are shown in black, and the Zn-finger domains are gray. 3T3 cells were transfected with *HA*-tagged *Mcm2* mutants along with *FLAG*-tagged *gp70*, and either left untreated (**B**) or treated with 1 μM doxorubicin for 24 h (**C**). The expression of the MCM2 mutants (**B**, **C**, left upper) and FLAG-gp70 (**B**, **C**, left middle) was confirmed in 3T3 cells. Cell lysates were subjected to a pull-down assay to detect the binding of MCM2-FL or MCM2 mutants to FLAG-gp70 (**B**, **C**, right panel).
doi:10.1371/journal.pone.0040129.g003

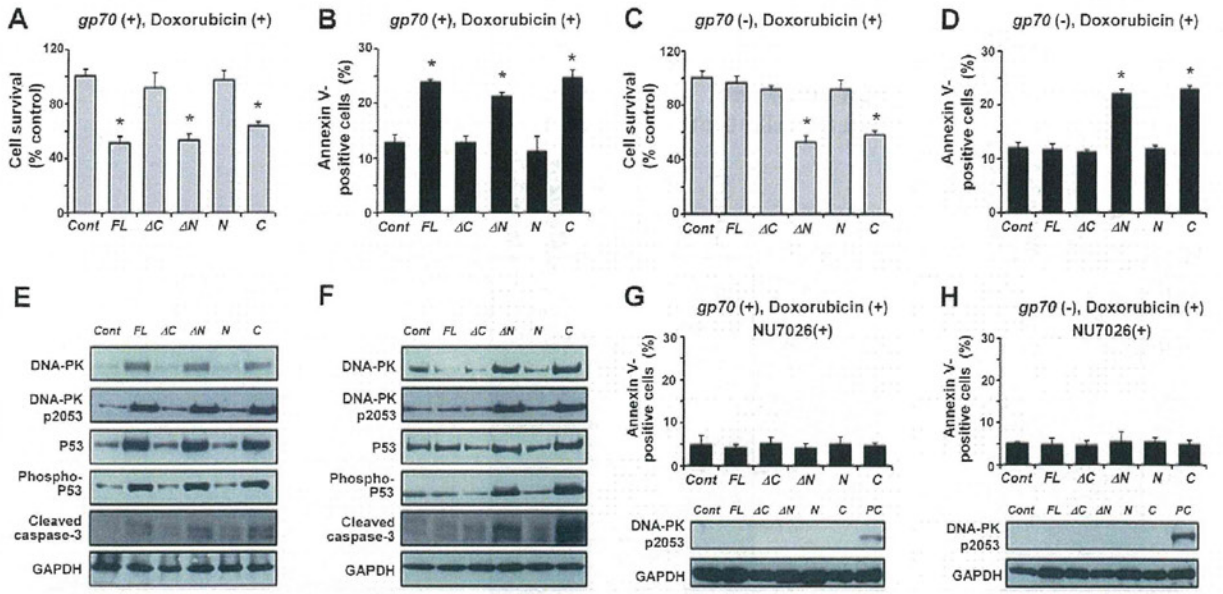

Figure 4. The C-terminal portion of MCM2 is important for apoptosis enhancement. 3T3 cells were co-taransfected with *gp70* and *Mcm2-FL* or the mutants (**A**, **B**) or transfected with *Mcm2-FL* or the mutants (**C**, **D**) and treated with 1 μM doxorubicin for 24 h. Cell survival (**A**, **C**) and apoptotic cell ratios (**B**, **D**) were determined using the MTT assay and annexin V-staining, respectively. Asterisks (*) indicate $p<0.01$ for control vs. mutant-transfected cells. In all panels, data represent the mean and 95% CI of 3 independent experiments. Western blot analysis of *gp70/Mcm2-FL*- and *gp70*/mutant-transfected 3T3 cells (**E**) and *Mcm2-FL*- and mutant-transfected 3T3 cells (**F**) after treatment with 1 μM doxorubicin for 24 h. The levels of DNA-PK, phospho-DNA-PK (pS2053), P53, phospho-P53, and cleaved caspase-3 are elevated in the groups with elevated apoptotic ratios. (**G**) 3T3 cells co-transfected with *gp70/Mcm2-FL* or *gp70*/mutants and (**H**) 3T3 cells transfected with *Mcm2-FL* or the mutants were pre-incubated with 10 μM NU7026, a DNA-PK-inhibitor, for 2 h and treated with 1 μM doxorubicin for 24 h. DNA-PK-pS2053 levels are substantially reduced in cells treated with the DNA-PK-inhibitor (**G** and **H**, bottom) compared to the levels in the absence of NU7026 (**E** and **F**, respectively). Whole cell lysates from *gp70*- and *Mcm2-FL*-transfected 3T3 cells after doxorubicin treatment are shown as a positive control (PC, **G** and **H**, bottom). Apoptotic cell ratios were determined with annexin V-staining (**G** and **H**, upper graph). In both panels, data represent the mean and 95% CI of three independent experiments.

doi:10.1371/journal.pone.0040129.g004

The gp70-MCM2 Complex is Localized in the Cytoplasm

The MCM2 protein contains an NLS in the N-terminal portion. Thus, MCM2 localizes to the nucleus when expressed in HeLa cells [47]. To investigate the cellular localization of MCM2, immunofluorescence was performed on 3T3 cells transfected with *Mcm2-FL* or mutated *Mcm2*, with or without *gp70* and treated with doxorubicin. In 3T3 cells singly transfected with *Mcm2-FL* or the mutants, MCM2-FL as well as MCM2-ΔC and MCM2-N were localized in the nucleus (Figure 6A). By contrast, MCM2-ΔN and MCM2-C lacking the NLS were localized in the cytoplasm (Figure 6A). In cells transfected with *gp70* plus *Mcm2-FL* or *gp70* plus mutated *Mcm2*, MCM2-FL and all the MCM2 deletion mutants were detected in the cytoplasm (Figure 6B). These results indicate that gp70 binding inhibits the nuclear translocation of MCM2 and show that MCM2 lacking an NLS remains in the cytoplasm. We confirmed that overexpression of gp70 and/or MCM2-FL or the mutants did not cause any significant changes in the cell-cycle profile of the transfected cells (Figure S5). Furthermore, the transfected gp70 induced the cytoplasmic localization of DNA-PK as well as MCM2 (Figure S6).

MCM2 has 2 NLS domains, NLS1 and NLS2. NLS2 but not NLS1 is required for the nuclear localization of mouse MCM2 [47]. Thus, to further examine the gp70-mediated inhibition of MCM2 nuclear translocation, we generated plasmids encoding HA-tagged MCM2 NLS deletions; deletion of NLS1 (MCM2-ΔNLS1), deletion of NLS2 (MCM2-ΔNLS1), and deletion of NLS1 to NLS2 (MCM2-ΔNLS1-2) (Figure 6C). 3T3 cells were transfected with these mutants and treated with doxorubicin, and apoptotic cell ratios were determined. The ratio was significantly increased in *Mcm2-ΔNLS2*- and *Mcm2-ΔNLS1-2*-transfected cells compared to the negative control. By contrast, *Mcm2-ΔNLS1*-transfected cells exhibited no increase in the number of apoptotic cells (Figure 6D). Furthermore, MCM2-ΔNLS1 was localized in the nucleus, whereas MCM2-ΔNLS2 and MCM2-ΔNLS1-2 were detected in the cytoplasm (Figure S7). These results indicate that deletion of NLS2 alters the subcellular localization of MCM2 and the apoptosis enhancement seen in the presence of the gp70-MCM2.

Induction of Leukemia cell Apoptosis by DNA-damage in FLV-infected Hosts

To determine whether C3H-derived leukemia cells exhibited enhanced apoptosis in response to gp70 and DNA-damage *in vivo*, SCID mice were intravenously transplanted with 8047 cells, inoculated with FLV, and treated with doxorubicin. As expected, the 8047 cell-containing liver samples from FLV-infected mice exhibited a stronger expression of *gp70* than those from uninfected mice (Figure 7A). Treatment with a low dose of doxorubicin caused significant enhancement of apoptosis in FLV-infected SCID mice but not in uninfected mice (Figure 7B, C). These results indicate that *gp70* overexpression and DNA-damage induction elicit significant apoptosis of C3H-derived leukemia cells *in vivo*.

Next, to investigate the subcellular localization of MCM2 in the transplanted 8047 cells from hepatic nodules, immunohistochem-

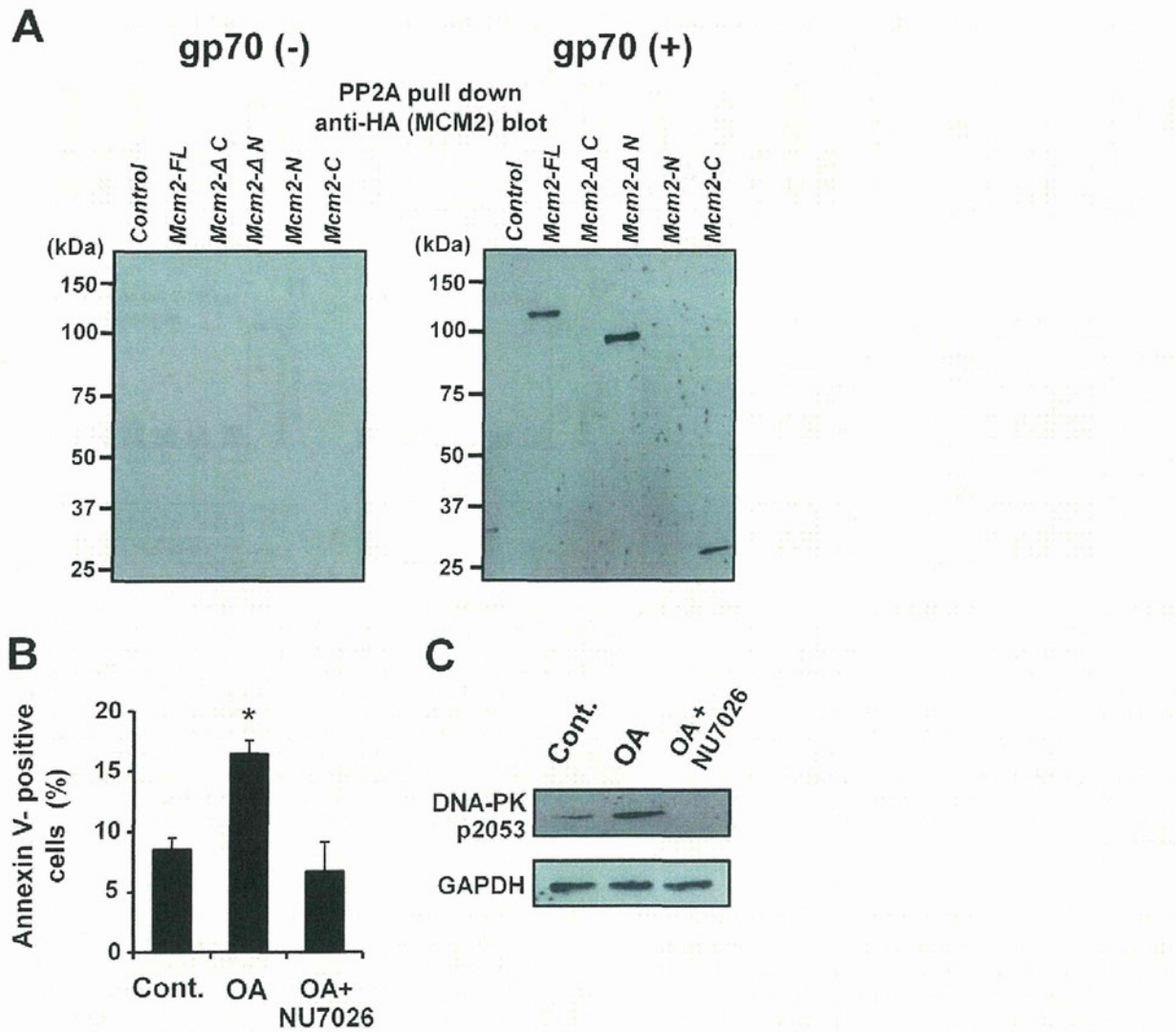

Figure 5. MCM2 (FL and mutants) interacts with PP2A. (**A**) The *Mcm2-FL*- or mutant-transfected 3T3 cells (left) and *gp70/Mcm2-FL*- or *gp70/mutants*-transfected 3T3 cells (right) were treated with 1 μM doxorubicin for 24 h. Cell lysates were subjected to a pull-down assay to detect the binding of MCM2-FL or the mutants to PP2A. (**B**) 3T3 cells were pre-incubated with 10 nM okadaic acid (OA) and 10 μM NU7026 for 2 h, and treated with 1 μM doxorubicin for 24 h. The apoptotic cell ratio was determined with annexin V-staining. Asterisk (*) indicates $p<0.01$ for control vs. mutant-transfected cells. Data represent the mean and 95% CI of 3 independent experiments. (**C**) Western blot analysis of 3T3 cells to detect phospho-DNA-PK. Note the significantly increased levels of DNA-PK-p2053 in OA-treated 3T3 cells, and the complete abrogation by NU7026.
doi:10.1371/journal.pone.0040129.g005

istry was performed. MCM2 was localized in the nucleus of 8047 cells in uninfected SCID mice (Figure 7D, top), whereas some 8047 cells exhibited cytoplasmic MCM2 in the FLV-infected mice (Figure 7D, bottom). Furthermore, the number of cells with cytoplasmic MCM2 was remarkably increased in FLV-infected doxorubicin-treated mice compared to FLV-infected PBS-treated mice (Figure 7D, bottom right and E).

A survival analysis was performed on mice treated with PBS or doxorubicin twice a week. FLV-infected and doxorubicin-treated mice exhibited a significant improvement in survival compared to the other groups (Figure 7F). These results suggest significant effects of cytoplasmic MCM2 on apoptosis induction in leukemia cells in the *in vivo* model. Although not so remarkable, FLV-infection alone prolonged the survival of 8047 cell-transplanted mice. The phenomenon may be caused by intrinsic host defense mechanisms such as innate immunity systems and inflammatory reactions by natural killer cells, neutrophils, monocyte/macrophages etc., against leukemia cells. The reactions may include reactive oxygen species or other stress signaling pathways associated with DNA-damage induction. Thus, the circulating leukemia cells may differ from the leukemia cells used *in vitro* experiments without any stimulation for DNA-damage.

Discussion

A novel strategy for controlling tumor cell growth is to target regulators of cellular proliferation/apoptosis. However, the cellular dynamics of non-tumor cells should not be influenced by